

## **The Foreign Object Damage Project of the PRDA V HCF Materials and Life Methods Program**

Mr. Phillip Gravett\*<sup>1</sup>, Dr. Richard Bellows<sup>2</sup>,  
Dr. Thomas Dunyak<sup>3</sup>, Dr. Douglas Herrmann<sup>4</sup>, Dr. Stephen Hudak Jr.<sup>5</sup>

\* Presenting Author (Team Leader)

<sup>1</sup>Pratt & Whitney, P.O. Box 109600 West Palm Beach, FL 33410-9600

<sup>2</sup>AlliedSignal Engines, P.O. Box 52181, Phoenix, AZ 85072-2181

<sup>3</sup>G.E. Aircraft Engines, One Neuman Way, Cincinnati, OH 45215-6301

<sup>4</sup>Allison Adv. Devl. Co., P.O. Box 420, Speed Code T-10B Indianapolis, IN 46206-0420

<sup>5</sup>Southwest Research Institute, P.O. Drawer 28510 San Antonio, TX 78228-0510

The USAF PRDA V Improved High Cycle Fatigue (HCF) Life Prediction program is a two year industry program chartered with the development of a damage tolerant based life prediction methodology toward the mitigation of HCF failures in titanium fan and compressor components of turbine engines. The Foreign Object Damage (FOD) task of the program seeks to eliminate HCF failures engendered by crack initiation and growth from the material damage zone associated with in-service FOD. The overall goal of the FOD task is the development of a design method by which relevant airfoil parameters (i.e. leading edge radius, taper, etc.) can be optimized for FOD tolerance. In addition, the method should allow for a more rigorous approach to the determination of nick and blend limits for management of FOD in the fleet.

The objective of the current program is to gain a better understanding of the effects of “typical” FOD on the HCF performance of 1<sup>st</sup> stage fan blades, and evaluate methods to predict the effects of FOD on crack initiation and growth. The approach to achieve this objective, illustrated schematically in Figure 1, encompasses experimental and analytic efforts. This approach began with an extensive data collection effort of in-service FOD occurrence to define “typical” FOD parameters which are deemed critical. Second, the durability of laboratory simulated FOD is being experimentally characterized, and the permanent deformation and residual stress from these FOD impacts are being analytically predicted. Finally, the experimental FOD durability and predicted residual stress

information is being used to evaluate the life models developed in the HCF/LCF task of the PRDA V program (1). In a follow on program, the developed methodology will be applied to more complex component tests, which more closely resemble turbine engine components.

In the initial stages of the program, existing data was collected on the relevant characteristics of FOD. In seeking information on the distribution of FOD sizes, shapes and occurrence rates observed in the fleet, it was determined that very little *systematic* data was available. As a result, a field inspection campaign was initiated to collect such data from over 600 FOD sites on over 8000 blades of various military engines. This included information on the occurrence rate per stage and blade span location, as well as the FOD size, depth, shape, notch root radius, and overall deformation. This information was presented in more detail at a previous HCF conference (2). Evaluation of this information guided the definition of the test and modeling program to focus on relatively small FOD located on the outboard section of a fan blade (Figure 2). This FOD could conceivably not be detected during preflight inspections and thus is critical to understand. A complete list of the FOD parameters to be evaluated is provided in Table 1.

To feasibly characterize the effects of numerous FOD parameters on blade tip durability in the laboratory, a flexural type “winged” specimen was designed for the FOD test program. The objective of the specimen design was to provide a simulated airfoil leading edge geometry and stress, which can be easily varied, while allowing the capability for high frequency fully reversed loading. Finite Element Analysis (FEA) of this specimen shows the simulated airfoil tip of the winged specimen closely approximates the geometry and stress field of a fan blade (Figure 3).

The second component of the FOD laboratory simulations is the method by which FOD is introduced. Various existing techniques were evaluated, considering damage state control and simulation of in-service FOD. The selected method uses an electric solenoid gun and a chisel shaped indenter to FOD specimens. Initially, this method is also being correlated to an air gun ballistic method with the winged laboratory specimen tests (Figure 4) for representative impact regions for both methods.

The third component of the laboratory simulation is the actual cyclic testing. The testing is being conducted on servo-hydraulic test machines in 4-point bending fixtures, with loading pins on both sides on the specimen to allow for fully reversed loading. The tests utilize electric potential drop (EPD) techniques to detect initiation, and selective heat tinting to document the crack size and crack front geometry during the test.

Evaluation of FOD methods with the winged specimen has initiated. Initial results show that baseline (undamaged) tests correlate well to smooth bar fatigue tests from the

HCF/LCF task. The addition of FOD damage results in a debit on  $1 \times 10^6$  cycle fatigue stress, but the effect seems to have a low sensitivity to FOD depth in the range tested. This is in spite of tearing seen in the  $\sim 0.020''$  FOD specimens. Figure 5 gives plots of the test results. The remaining test program will seek to characterize the HCF response of the FOD specimens for model development and calibration for the parameters defined in Table 1.

In a parallel effort, a diamond cross section tensile (DCT) specimen with a quasi-static servo-indenter FOD method is being evaluated. This effort has tested baseline (undamaged) and FOD damaged specimens to determine the repeatability of the FOD damage introduction and the effect of FOD on initiation based fatigue life. Initial test results show good correlation between baseline DCT and smooth bar baseline tests, and that  $0.025''$  depth FOD shows gross deformation and has greatest effect on life. Figure 6 provides FOD deformation and test results.

In parallel to the FOD testing effort, the dynamic impact code DYNA 3D is being used to potentially develop the capability to predict FOD damage through numerical simulation. This will offer a method to determine the effective geometric stress concentration, associated stress field and residual stress state such that the local stresses and strains during fatigue loading can be predicted for input into an HCF/LCF fatigue model. It is envisioned that these simulations will allow sensitivity studies to be performed with respect to design variables, such as leading edge radius, to evaluate the damage state and provide predictive information for conditions not tested.

In tandem with the DYNA 3D simulations, analytic techniques are being developed for the prediction of FOD HCF capability. Approaches are currently being explored for evaluating the geometric stress concentrations and the associated stress gradient and crack stress intensity (K) for FOD engendered notches, including effects of notch sensitivity and residual stress. This information is necessary to understanding the material state in the vicinity of FOD damage, and how subsequent cyclic loading stresses interact with the FOD damage.

With the effects of the FOD event on the stress state of the leading edge predicted, the initiation (1), crack growth (1), and worst case notch (WCN) (3) models developed in the HCF/LCF task will be evaluated and correlated with the laboratory test results. The HCF/LCF initiation models, both stress invariant and critical plane, will be evaluated with the FOD durability testing on the winged specimen design. Likewise, the HCF/LCF crack growth models will be evaluated with the FOD durability testing to define threshold crack initiation based criteria. The accuracy and application of these models will be assessed, and the most appropriate chosen for further evaluation in following programs. The WCN model will be evaluated to assess the applicability to the

establishment of improved blade FOD accept/reject criteria and blend limits. In following programs, these models will be used to predict the effect of damage level on initiation in bench tested fan and compressor blades at elevated temperatures.

Reference:

1. DeLanauville, Robert, “The HCF/LCF Interaction Project in the PRDA V HCF Materials and Life Methods Program,” *4th National Turbine Engine High Cycle Fatigue Conference*, Monterey, CA, 9 February 1999.
2. Walls, Dr. David, “The Foreign Object Damage Project in the PRDA V HCF Materials and Life Methods Program,” *3rd National Turbine Engine High Cycle Fatigue Conference*, San Antonio, TX, 4 February 1998.
3. Hudak, Dr. Stephen, “A Damage Tolerance Approach to FOD based Propagation and Arrest of Cracks at Notches,” *4th National Turbine Engine High Cycle Fatigue Conference*, Monterey, CA, 11 February 1999.

**Table 1. FOD parameters and range for FOD characterization test program.**

FOD Parameter	Range
FOD depth	0.005” - 0.025”
FOD incidence angles	0°, 30°, and 90°
Loading R-ratio	-1.0 (simulate blade tip) 0.5 (simulate mid-span)
Leading edge diameter	0.010” (aerodynamic ) 0.030” (robust)

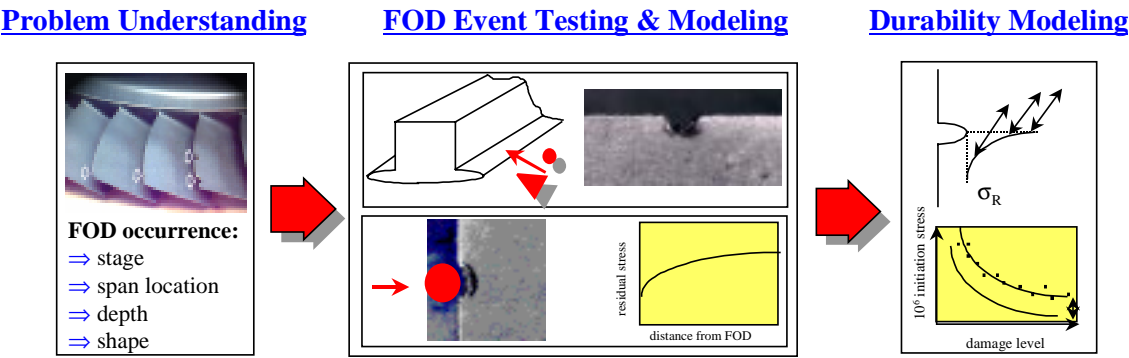
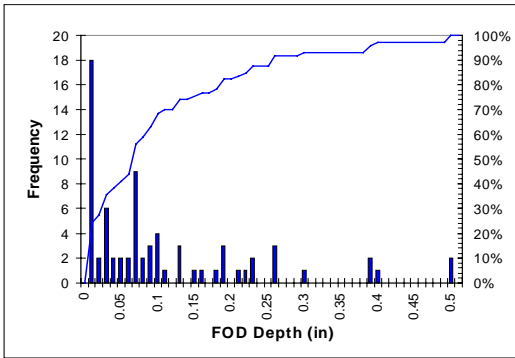
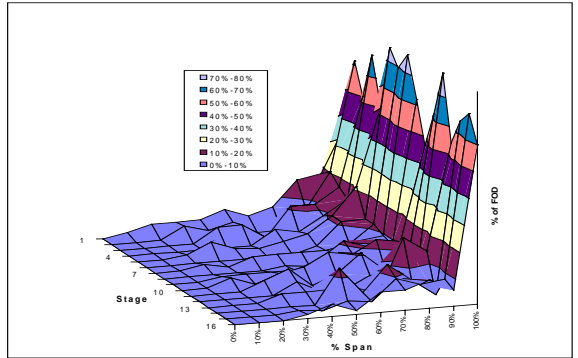


**Figure 1. A Schematic representation of the overall approach of the FOD effort.**

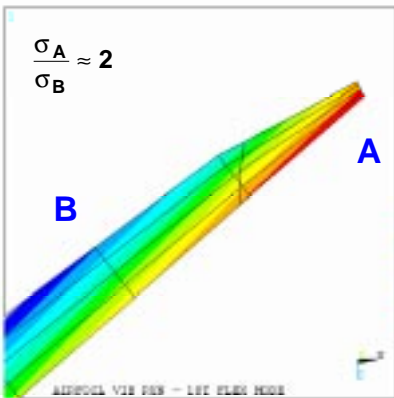


a.

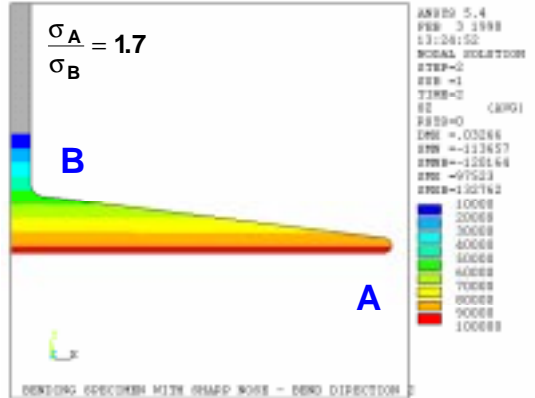


b.

**Figure 2. Distribution of in service FOD by depth (a) and span wise location (b).**

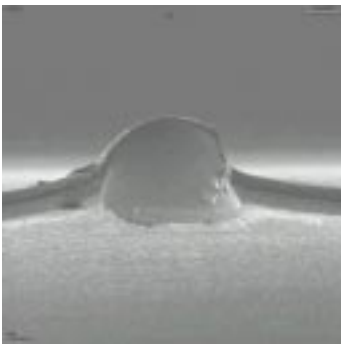


a.

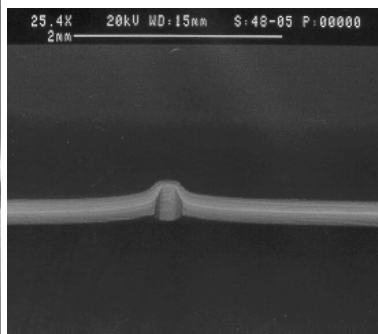


b.

**Figure 3. A Comparison of the fan blade (a) and winged specimen (b) FEA modeling.**



a.

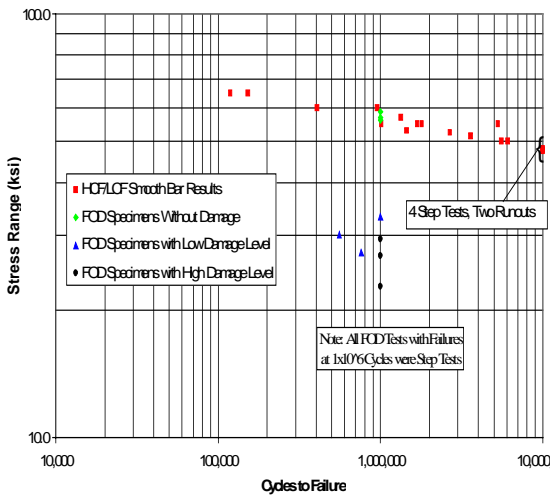


b.

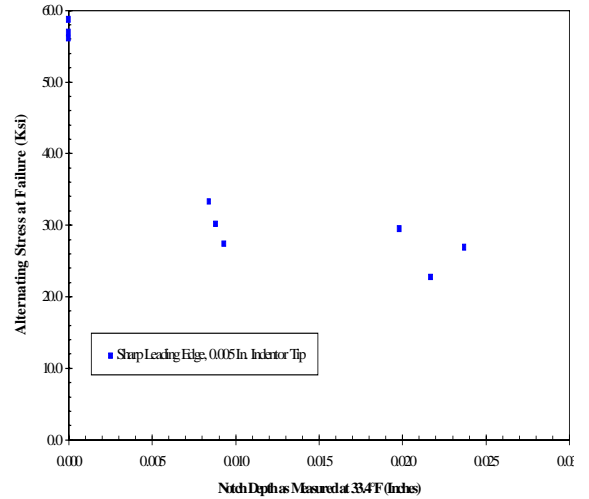


c.

**Figure 4. FOD damage sites from ballistic impact (a) and solenoid gun (chisel indenter) low damage (b) and high damage (c) methods.**

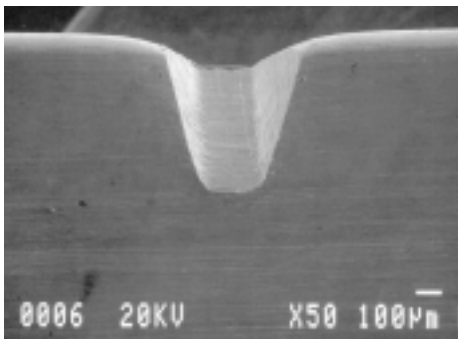


a.

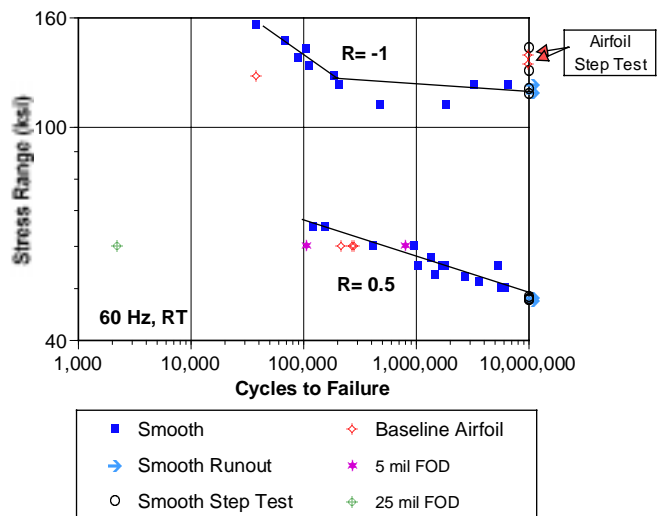


b.

**Figure 5. Initial winged specimen test stress vs. cycles (a) and stress vs. FOD depth (b) plots.**



a.



b.

**Figure 6. Initial Diamond Cross section Tensile specimen FOD (a) and durability test results (b).**

## **A Damage Tolerance Approach to FOD Based on the “Worst Case Notch” Concept**

Dr. Stephen J. Hudak, Jr.\*, Dr. G. Graham Chell  
Mr. Timothy S. Rennick, Dr. R. Craig McClung, and Dr. David L. Davidson,  
Southwest Research Institute  
6220 Culebra Rd.  
San Antonio, TX 78238-5166

### **INTRODUCTION**

The occurrence of foreign object damage (FOD) can significantly reduce the resistance of turbine blades to high cycle fatigue (HCF). Thus, FOD needs to be explicitly accounted for in designing against HCF. In so doing, two elements of the problem need to be addressed—the geometric stress concentration effect of the FOD shape, as well as the residual stresses induced by the FOD impact. The current paper is focused on the geometrical influence of the FOD stress concentration on HCF behavior. The methods described herein can be readily extended to include the influence of the FOD residual stresses, once these stresses are known. However, the precise definition of these residual stresses remains problematical because of the high gradients and small size scales over which these residual stresses occur. Ongoing research within the overall PRDA V HCF Program is addressing this problem.

The severity of FOD-induced notches can vary significantly, depending on their depth and root radius—both of which can vary appreciably [1-2]. It is well known from classical fatigue research that sharp notches are less damaging than one might anticipate based on their high theoretical elastic stress concentration factors and several empirical approaches have attempted to account for this effect [for example, see Ref. 3]. More recently, it has been suggested that this effect is fundamentally related to the initiation, propagation and arrest of microcracks in the presence of the high stress gradients associated with sharp notches. Specifically, sharp notches tend to initiate microcracks that eventually arrest as they grow out of the influence of the highly concentrated notch stress field [4-6]. For some time, these observations appeared to be inconsistent with classical fracture mechanics solutions of cracks growing from notches since such solutions predict increasing crack driving forces—and thus continued crack

growth—rather than arrest. However, recent understanding of the unique behavior of small fatigue cracks has provided an explanation of this crack arrest behavior [5-7], and initial success using fracture mechanics to estimate the propagation and arrest of small cracks at notches has motivated the present work [6]. If the occurrence of these non-propagating cracks can be confidently predicted, this dormant state can be taken advantage of in HCF design.

## “WORST CASE NOTCH” CONCEPT

Treating small crack effects and the associated conditions for non-propagation of cracks in the stress gradients of notches can lead to the definition of a limiting “worst-case notch”. Such an approach could provide a viable engineering solution to the problem of dealing with the large variation in FOD-notch geometry that is encountered in turbine engine blades. Initial developments along these lines have demonstrated success in treating the variation in weld-toe root radii, and their consequent effects on the HCF behavior of offshore structures [8, 9].

The “worst case notch” concept is illustrated in Figure 1 where the nominally applied threshold stress for a notched member is shown as a function of both the elastic stress concentration factor  $k_t$  and crack size ‘a’. As can be seen in Figure 1a, the threshold stress, computed by dividing the endurance limit ( $\Delta\sigma_e$ ) by  $k_t$ , continually decreases with increasing  $k_t$  (and notch severity). However, worst case notch theory predicts a limiting  $k_t$ , termed  $k_w$ , above which further increases in  $k_t$  no longer result in decreases in the threshold stress due to the occurrence of crack arrest and non-propagating cracks. These curves define boundaries separating three distinct regimes where: 1) crack initiation will not occur; 2) crack initiation will occur, followed by crack arrest; and 3) crack initiation followed by crack growth will result in failure of the notched member. These same regimes are shown as a function of crack size in Figure 1b, for a fixed notch depth and three different notch root radii,  $\rho_1$ ,  $\rho_2$ ,  $\rho_3$ . As indicated in Figure 1b, the threshold stress increases as the radius increases and there exists a limiting radius,  $\rho_w$ , above which crack arrest can not occur. In general, the notch severity will be a function of both the notch depth,  $b$ , and the notch root radius,  $\rho$ , thus the phase boundaries in Figure 1b will move with varying notch depth. However, since this dependence can be computed using fracture mechanics, the worst case notch can always be defined. The goal of the worst case notch approach is to quantify these dependencies and thereby treat the fatigue notch problem in a systematic fashion that can be employed in design.

In general, the threshold stress is a function of the FOD-notch geometry, loading mode, and material variables as follows:

$$\Delta\sigma_{th} = \Delta\sigma_{th}(k_t[b, \rho], a, a_0, \lambda) \quad [1]$$



where  $\lambda$  is a parameter which depends on loading mode (e.g., tension vs bending) and  $a_0$  is the small crack parameter suggested by El Haddad et. al. [10] given by:

$$a_0 = 1/\pi(\Delta K_{th}/F\Delta\sigma_e)^2 \quad [2]$$

where  $\Delta K_{th}$  is the threshold stress intensity factor range for measurable fatigue crack growth,  $\Delta\sigma_e$  is the smooth bar endurance limit, and  $F$  is the geometry factor for a thumbnail crack in a smooth bar given by  $1.12 (2/\pi) = 0.713$ .

Although there has been extensive debate regarding the physical significance of  $a_0$  as a material constant, we interpret it here as a parameter which interpolates between the smooth and cracked specimen responses in terms of a crack-length-dependent, small-crack threshold stress intensity,  $\Delta K_{th}(a)$ , given as:

$$\Delta K_{th}(a) = \Delta K_{th}(R) \left[ \frac{a}{a + a_0} \right]^{1/2} \quad [3]$$

where  $\Delta K_{th}(R)$  is the long crack threshold, which depends on load ratio ( $R$ ).

## MECHANICS OF NOTCHES

The stress intensity factors (SIFs) for cracks emanating from FOD are needed for fatigue crack growth/arrest analyses and for determining worst case notch (WCN) scenarios. In the present work, the SIF is calculated from the stress ahead of the FOD in the absence of a crack,  $\sigma_{FOD}(x/\rho, k_t[b,\rho])$ , using the weight function approach, where the distance  $x$  is measured from the root of the FOD. If  $W(a,x,a/\rho,k_t[b,\rho])$  is the weight function for a crack at a notch, then the SIF,  $K(a, a/\rho, k_t[b,\rho])$  for a crack of depth,  $a$ , is given by:

$$K_{FOD}(a, a/\rho, k_t[b,\rho]) = \int_0^a W(a, x, a/\rho, k_t[b,\rho]) \sigma_{FOD}(x/\rho, k_t[b,\rho]) dx \quad [4]$$

In general,  $\sigma_{FOD}$  will include a contribution from residual stresses induced during the formation of the FOD, as well as the local stress resulting from remote blade loading. The weight function,  $W$ , is estimated from the SIF solutions for cracks at surface notches subjected to remote uniform tension [11] using the reference solution approach. These SIF solutions were represented parametrically in the form:

$$K_{notch}(a, a/\rho, \rho/b) = \sigma\sqrt{\pi a}F(s, \rho/b) \quad [5]$$

where  $\sigma$  is the remote stress, and  $s = a/(a + b)$ .  $W$  in Eq [4] was derived using the relationship:

$$F(s, \rho/b) = \frac{\int_0^a W(a, x, a/\rho, k_t[b, \rho]) \sigma_{\text{notch}}(x/\rho, k_t[b, \rho]) dx}{\sigma \sqrt{\pi a}} \quad [6]$$

The following parametric equations is used for  $k_t$

$$k_t = f(\rho/b) \left[ 1 + \frac{2K(b)}{1.122\sqrt{\pi\rho}} \right] \quad [7]$$

where

$$f(\rho/b) = 1 + \frac{0.122}{(1 + \sqrt{\rho/b})^2} \quad [8]$$

is a free surface correction factor given in Tada et.al. [11]. The SIF,  $K(b)$ , is evaluated using the remote stress and the crack size is taken to be the depth of the notch.

The following expression, derived by Amstutz and Seeger [12], is used for  $\sigma_{\text{notch}}(x/\rho, k_t)$  in Eq. [6]:

$$\sigma_{\text{notch}}(x/\rho, k_t) = \sigma_t \left[ 1 + \frac{k_t - 1}{t(1 + \phi x/\rho)^\psi} \right] \quad [9]$$

where

$$\phi = 3.226 - \frac{2.706}{(k_t - 0.9224)^{0.5018}}, \quad 2 < k_t < 50 \quad [10a]$$

$$\phi = 0.226 + 0.394(k_t - 1)^{3.0457}, \quad 1 < k_t < 2 \quad [10b]$$

$$\psi = \frac{1}{\phi} \frac{2k_t + 1}{k_t - 1}$$

## COMPARISON OF MODEL PREDICTIONS AND EXPERIMENTS

In order to assess the viability of the “worst case notch” model, predictions of the model were compared with available notched HCF data from the literature, including both historical data on steel [4,5], and recently acquired data on Ti-6Al-4V from the PRDA V HCF Program [13].

Figure 2 shows that the prediction of the various threshold stress ranges as a function of the elastic stress concentration factor are in good agreement with the measurements of Frost et. al. [4,5] on notched mild-steel specimens. The value of  $a_0$  used in these predictions for mild steel was 0.45 mm. Note that both the threshold stress for initiation/arrest and for complete failure of the specimens are in reasonable agreement with the measurements. Moreover, the limiting threshold stress range, corresponding to the worst case notch, is correctly predicted to be dependent on specimen geometry. The cracked round bar (CRB) specimen was modeled as a surface crack growing from the notch, while the double edge notch plate (DENP) specimen was modeled as a through-thickness crack in a plate. The differences in crack and specimen geometry give rise to the lower threshold stress for the DENP specimen, in agreement with the trend in the measured data.

Figure 3 shows the predicted variation in the threshold stress as a function of crack depth for the case of steel containing notches of constant depth and three different notch root radii. These results clearly illustrate the increased tendency for crack arrest at the sharper notches as the result of the well-defined local maximum in the curve for the sharpest notch. This feature of the model is a direct consequence of the manner in which the small crack effect is represented. Specifically, Figure 4 shows three different assumptions regarding the treatment of small crack effects. The solid curve is for the case where small cracks are assumed to have a  $\Delta K_{th}$  that is crack size dependent as described by Eq. [3]. As can be seen, this assumption leads to markedly different predictions compared to the case where an equivalent initial flaw size is assumed—that is, ‘a’ is replaced by a  $+a_0$  in every crack size term in Eq. [5]. As shown in Figure 4, the equivalent crack size assumption is similar to assuming there is no small crack effect ( $a_0 = 0$ ) in that neither interpretation predicts crack arrest.

As demonstrated by Topper and El Haddad, analyses of this type enable the fatigue notch reduction factors ( $k_f$ ) to be predicted based on fracture mechanics concepts. For the case of FOD—which can induce relatively sharp notches—this approach would appear to be superior to the classical approach of defining an empirical relationship between  $k_f$  and  $k_t$ . This notion is demonstrated by the model predictions in Figure 5 which show a family of threshold stress versus crack size curves for various combinations of notch depth and radii, all corresponding to the same  $k_t$  of 7.5. These results clearly demonstrate that the crack arrest capability of notches depends both on their radii and

depth—as well as on the crack and specimen geometry, as previously shown in Figure 2. Thus, simple empirical correlations between  $k_f$  and  $k_t$  are bound to break down in certain regimes—particularly for deep, sharp notches of the type that can be produced by FOD.

Figures 6 and 7 show model predictions for  $R = -1$  and  $0.5$ , respectively, compared with corresponding HCF data on Ti-6Al-4V [13]. The model predictions depend on  $R$  through the  $R$ -dependence of both the endurance limit and the crack growth threshold, both of which govern  $a_0$ . Although the predictions are in good agreement with the data, they do not provide a very robust assessment of the viability of the model for Ti-alloys since the low  $k_t$  data shown are in the region governed by  $\Delta\sigma_{th}/k_t$ . Additional testing is planned with sharper notches to verify the region where crack arrest is predicted.

Figure 8 illustrates the expected  $\Delta\sigma_{th}$  trend predicted from the “worst case notch theory” and compares this with various levels of applied stress. These results illustrate a possible scenario by which “interactions” between HCF and LCF (low cycle fatigue) can occur. For the case shown, initial HCF loading at a relatively low applied stress range results in the initiation, growth and arrest of a crack. This is followed by LCF loading at a higher stress range that results in further crack growth. Nevertheless, subsequent HCF loading results in no additional HCF damage since the applied stress range is still below  $\Delta\sigma_{th}$ . At this point, a tolerable margin of LCF crack growth still exists. However, as illustrated in Figure 8, further LCF crack growth beyond the crack arrest regime could eventually trigger additional HCF propagation which could result in component failure.

## CONCLUDING REMARKS

Initial comparisons between model predictions and experiments on steel and titanium alloy provide encouragement that the “worst case notch” approach may be useful for HCF design of components subjected to FOD. This approach would be particularly useful for design against FOD with highly variable root radii, since the existence of the “worst case” limiting value of  $\Delta\sigma_{th}$  precludes the need for detailed knowledge of the FOD root radii. Although this approach requires small crack effects to be treated, it is otherwise fully compatible with existing LCF design methods. Also, since the concentrated stresses and stress gradients are similar in notches and in fretting fatigue, the worst case notch concepts can be extended by analogy to the treatment of fretting fatigue as discussed elsewhere in this proceedings [14].

## ACKNOWLEDGEMENT

This material is based upon work supported by the U. S. Air Force Research Laboratory (AFRL) under Contract No. F33615-96-C-5269 managed by the University of Dayton Research Institute. The support and encouragement of Mr. Joseph Burns and Dr. Ted Nicholas of AFRL, as well as the HCF Damage Tolerance Team, are greatly appreciated.

## REFERENCES

1. J. M. Larsen, B. D. Worth, C. G. Annis, Jr., and F. K. Haake, "An Assessment of the Role of Near-Threshold Crack Growth in High-Cycle Fatigue Life Predictions of Aerospace Titanium Alloys Under Turbine Engine Spectra," *International Journal of Fracture*, Vol. 80, 1996, pp. 237-255.
2. S. J. Hudak, Jr., R. C. McClung, K. S. Chan, G. G. Chell, and D. L. Davidson, "High Cycle Fatigue of Turbine Engine Materials," SwRI's Annual Interim Technical Report to UDRI under PRDA 95, January 15, 1998.
3. R. E. Peterson, "*Stress Concentration Factors*," John Wiley and Sons, New York, 1974.
4. N. E. Frost and D. S. Dugdale, *Journal of the Mechanics and Physics of Solids*, Vol. 5, 1957, p.182.
5. *Metal Fatigue*, N. E. Frost, K. J. Marsh, and L. P. Pook, Clarendon Press, Oxford, 1974.
6. T. H. Topper and M. H. El Haddad, "Fatigue Strength Predictions of Notches Based on Fracture Mechanics," *Fatigue Thresholds: Fundamentals and Engineering Applications*, Engineering Materials Advisory Services, LTD, Warley, U.K., 1982.
7. S. J. Hudak, Jr., "Small Crack Behavior and the Prediction of Fatigue Life," *ASME Trans., Journal of Engineering Materials and Technology*, Vol. 103, 1982, p. 26.
8. F. V. Lawrence, "Predicting the Fatigue Resistance of Welds," *Annual Review of Material Science*, Vol. 11, 1981, p. 401.
9. S. J. Hudak, Jr., O. H. Burnside, and K. S. Chan, "Analysis of Corrosion Fatigue Crack Growth in Tubular Joints," *ASME Trans., Journal of Energy Resource Technology*, Vol. 107, 1985.
10. M. H. El Haddad, K. N. Smith, and T. H. Topper. Fatigue Crack Propagation of Short Cracks," *ASME J. of Engr. Materials. & Tech.*, Vol. 101, 1979, p. 42.
11. H. Tada, P. Paris, and G. Irwin, *The Stress Analysis of Cracks Handbook*, 2nd Edition, Del. Research Corporation, 1985.
12. H. Amstutz and T. Seeger, "Accurate and Approximate Elastic Stress Distribution in the Vicinity of Notches in Plates Under Tension" Unpublished Results. (referenced in G. Savaidis, M. Dankert, and T. Seeger, "An Analytical Procedure for Predicting Opening Loads of Cracks at Notches. Fatigue," *Fract. Engng Mater. Struct.*, Vol. 18, No. 4, pp. 425-442, 1995).
13. R. deLaneuville, J. Sheldon, K. Bain, D. Slavik, R. Bellows, R. C. McClung, D. L. Davidson, and D. Herrman, "The HCF/LCF Interaction Project in the PRDA V HCF Materials and Life Methods Program," Proceedings of the 4<sup>th</sup> National Turbine Engine High Cycle Fatigue Conference, Monterey, CA, February, 1999.
14. K. S. Chan, Y-D. Lee, D. L. Davidson, and S. J. Hudak, Jr., "A Fracture Mechanics Approach to High Cycle Fretting Fatigue Based on the Worst Case Fret Concept," Proceedings of the 4<sup>th</sup> National Turbine Engine High Cycle Fatigue Conference, Monterey, CA, February, 1999.

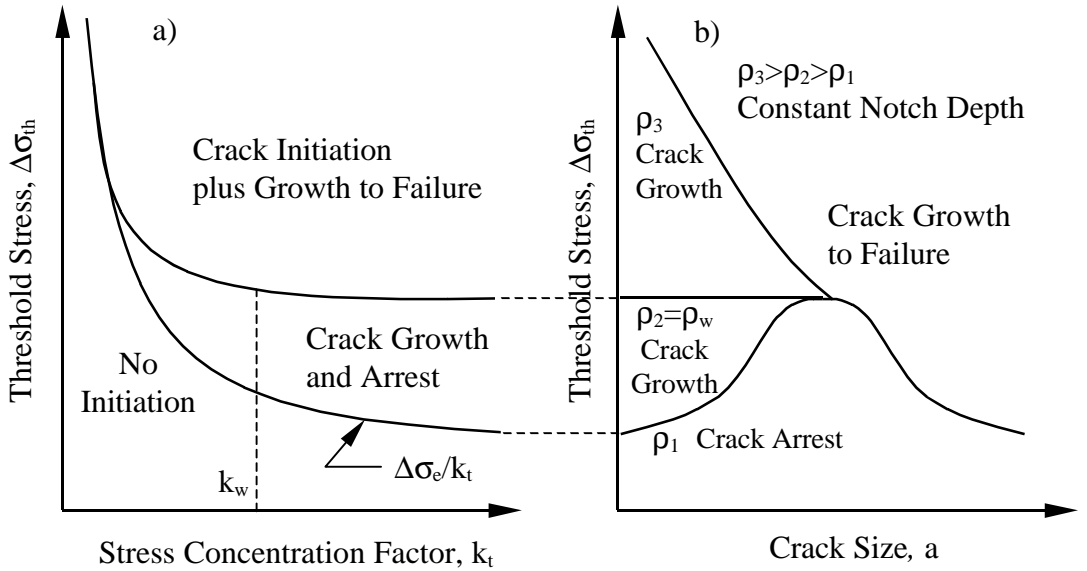


Figure 1. Schematic illustration of the “worst case notch” concept. The “worst case notch” can be defined in terms of either a limiting  $k_t$ , termed  $k_w$ , or, for the case of a constant notch depth, a limiting notch root radius  $\rho_w$ . In general, the “worst case notch” will depend on notch depth and radius in a manner that can be predicted using fracture mechanics analysis.

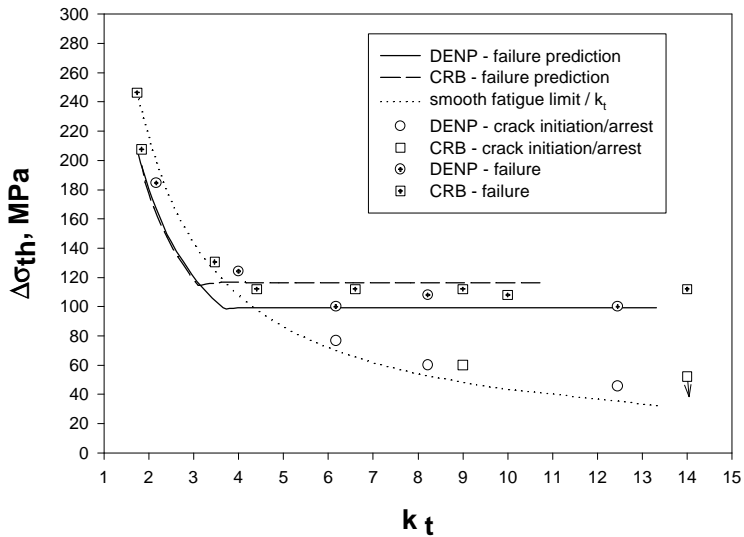


Figure 2. Comparison of “worst case notch” predictions with notched steel HCF data of Refs. [4,5] showing good agreement including correct prediction of specimen geometry effects.

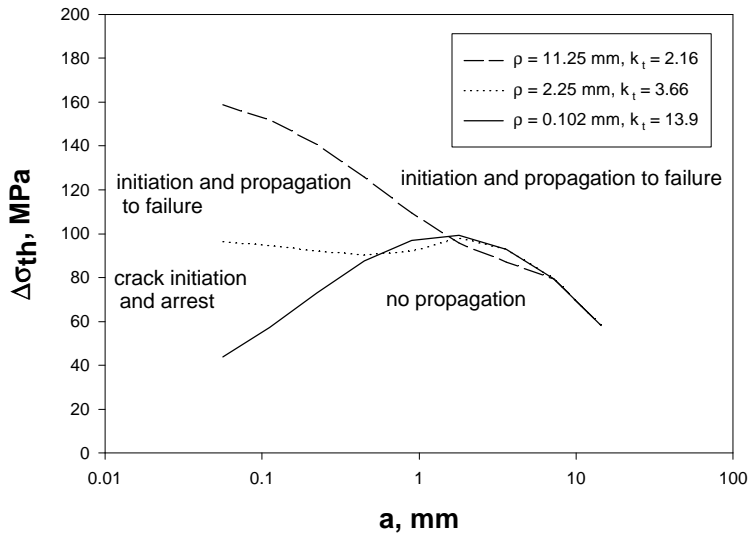


Figure 3. Predicted variation of threshold stress versus crack size for several notch radii and a constant notch depth in steel illustrating the tendency for crack arrest with increasing notch sharpness.

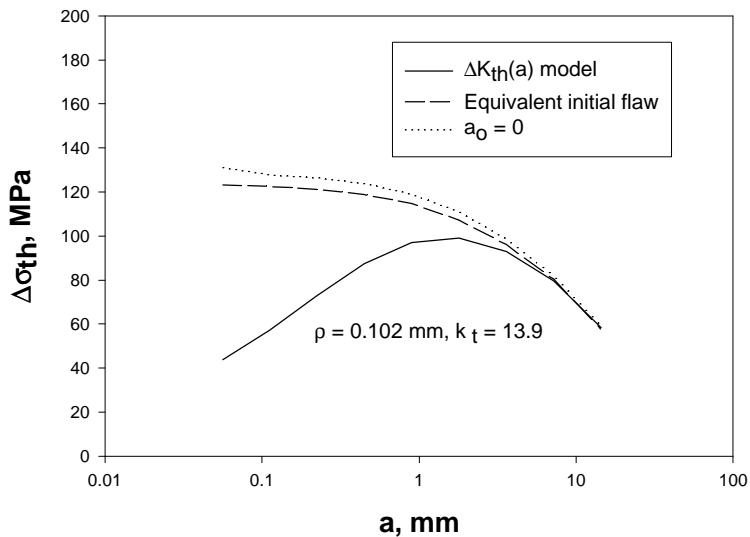


Figure 4. Predicted variation in threshold stress versus crack size in steel depending on different methods of treating small crack effects. The notion that  $\Delta K_{th}$  is a function of crack size predicts crack arrest in best agreement with HCF data in sharply notched specimens.

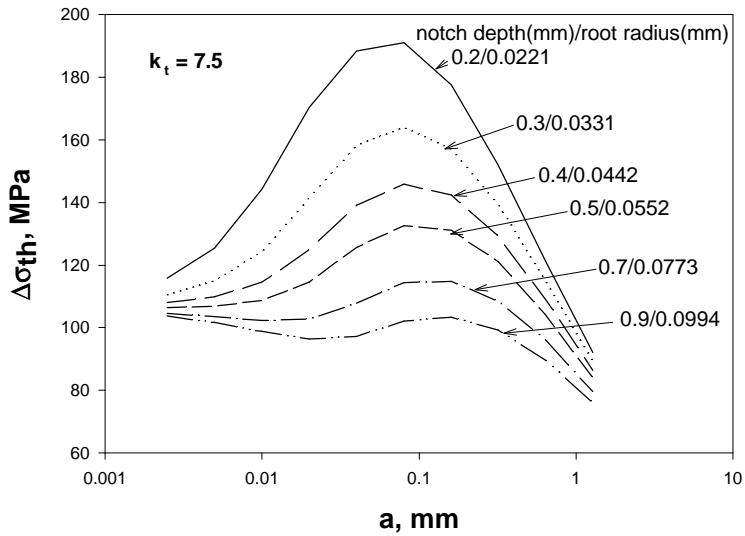


Figure 5. Predicted threshold stress versus crack size in steel for varying notch depths and radii, each giving the same  $k_t$  of 7.5. Results illustrate that  $k_t$  alone is not adequate to describe the HCF behavior of notched members.

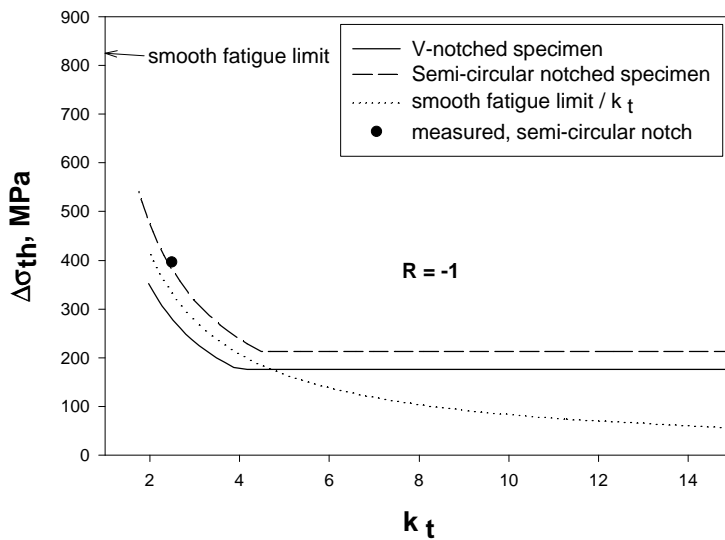


Figure 6. Comparison of 'worst case notch' predictions and notched HCF data of Ref. [13] for Ti-6Al-4V at  $R = -1$ .



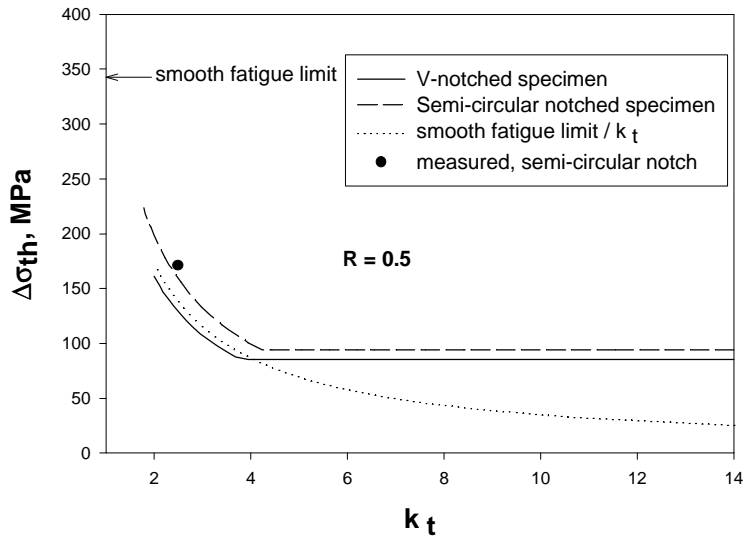


Figure 7. Comparison of ‘worst case notch’ predictions and notched HCF data of Ref. [13] for Ti-6Al-4V at  $R = 0.5$ .

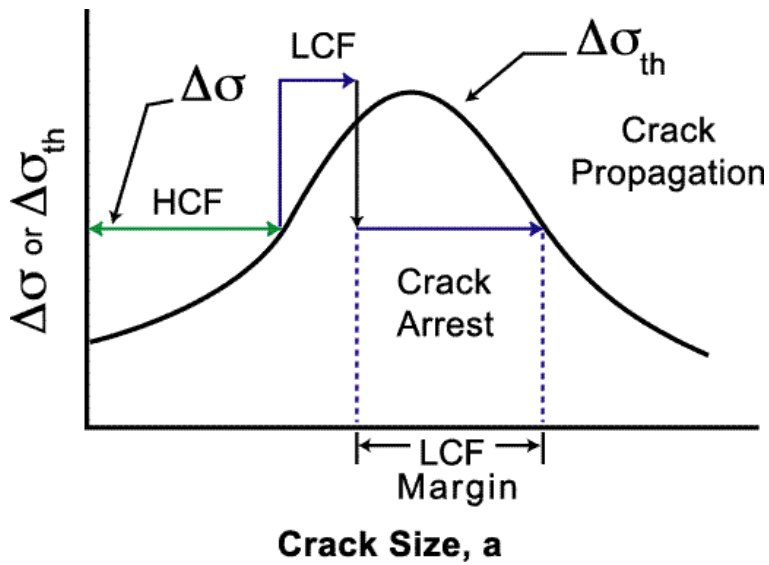


Figure 8. Postulated HCF/LCF “interaction” in notched members.

## Notch Size Effects and LCF/HCF Interactions in Ti-6Al-4V<sup>†</sup>

Dr. David Lanning\* and Col. George K. Haritos, Ph.D.  
Air Force Institute of Technology  
2950 P Street  
Wright-Patterson AFB, OH 45433-7765

Dr. Theodore Nicholas  
Air Force Research Laboratory  
2230 Tenth Street, Ste. 1  
Wright-Patterson AFB, OH 45433-7817

Notch size effects in two Ti-6Al-4V specimen geometries under high cycle fatigue loading and the influence of combined LCF/HCF (low cycle fatigue/high cycle fatigue) loadings are investigated. Flat dogbone specimens with two sizes of notches, having elastic stress concentration factors of  $K_t = 2.7$ , were cycled to generate points on a Haigh diagram for a constant life of  $10^6$  fatigue cycles using a step loading technique. The loading conditions required for failure are compared to those of circumferentially notched cylindrical specimens for the same fatigue life, in terms of the stress state at the notch root both with and without stress redistribution due to plastic deformation. Cylindrical fatigue specimens, with two sizes of circumferential V-notches where  $K_t = 2.7$ , were initially cycled under LCF loading conditions. The HCF fatigue limit was subsequently determined using the step loading method, and compared to baseline HCF fatigue limits without prior LCF damage.

Previous work has shown that one of the controlling parameters of the notch size effect in Ti-6Al-4V is the product form (Lanning et al., 1999), and that there was little notch size effect in a Ti-6Al-4V forged plate product form for a range of notch sizes in cylindrical specimens having an elastic stress concentration factor of  $K_t = 2.7$ . All specimens in the present study were taken from the same Ti-

---

<sup>†</sup> The views expressed in this article are those of the authors and do not reflect the official policy or position of the United States Air Force, Department of Defense, or the U.S. Government.

6Al-4V forged plate product form. Mechanical properties of the Ti-6Al-4V plate are provided in Table 1 for two strain rates, and details of the forged plate heat treatment may be found elsewhere (Lanning et al., 1999).

Flat dogbone specimens were machined with opposite V-notches. Diagrams of the flat dogbone specimens and circumferentially notched cylindrical specimens used in this investigation are shown in Figure 1, and the corresponding dimensions are provided in Tables 2 and 3. All notch sizes from both geometries have elastic stress concentration factors of approximately  $K_t = 2.7$  (Nisitani and Noda, 1984; Peterson, 1974). The out-of-plane stress component of the biaxial stress state at the notch root, halfway through the thickness, is less than the circumferential stress at the surface of the notch root in the cylindrical specimens. A step loading method for generating points on the Haigh (Goodman) diagram for a constant life of  $10^6$  fatigue cycles was used. This method has been verified for unnotched Ti-6Al-4V specimens at  $10^7$  cycles (Maxwell et al., 1998) and notched Ti-6Al-4V specimens at  $10^6$  cycles (Lanning et al., 1999). All specimens were cycled at a frequency of 50 Hz, and at stress ratios of  $R = 0.1, 0.5$ , and  $0.8$ .

The Haigh diagram for the V-notched flat specimens is shown in Figure 2. A notch size effect is evident, where the smaller notch requires higher stresses to produce failure at  $10^6$  cycles for a given stress ratio. Figure 3 provides a comparison between the results for both flat and cylindrical notched specimen geometries. While the notch size effect is evident in the flat specimens, it does not appear to be significant in the cylindrical specimens, for the range of notch sizes tested. The fatigue notch factors illustrate the notch size effect, and are provided in Table 4.

Three-dimensional elastic finite element models of the flat specimen geometries were solved with NASTRAN to characterize the biaxial stress state along the surface of the notch root. Figure 4 shows the calculated stress distribution along the root of the notch for both the small and large notch geometries, normalized with the average stress across the reduced cross-section. The von Mises effective stress for the cylindrical specimens was estimated to be  $S_{eff} = 0.88S_x$  for all three notch sizes, where  $S_x$  is the axial stress in the direction of loading (Leven, 1955). The data from the Haigh diagram in Figure 3 has been replotted in terms of effective mean and alternating stresses in Figure 5. While the use of effective stresses may collapse the data somewhat towards a single curve, it is not clear that this can substantially improve HCF lifetime predictions.

Additional insight into the notch behavior under HCF loadings may be gained by solving for the stress state and local stress ratio in the vicinity of the notch root after stress redistribution occurs due to plasticity. Elastic perfectly-plastic, two-dimensional, plane strain finite element models (FEM) of the flat notched specimens were solved with ABAQUS to provide the stress states at the

points of maximum and minimum loading during the fatigue cycle. The von Mises yielding criterion was used in the elastic-plastic solution, using the mechanical properties obtained from tensile tests at elevated strain rates ( $0.05 \text{ s}^{-1}$ ) given in Table 1. Significant stress redistribution occurs at  $R = 0.8$ , where the notch root experiences a local stress ratio of around  $R = 0.6$ . Only minor redistribution occurs at an applied stress ratio of  $R = 0.5$ . A comparison between the notch tip stresses after stress redistribution occurs, and the elastic notch tip stresses if no redistribution were to occur is shown in Figure 6. Both mean and alternating stresses are plotted as effective quantities. Unnotched specimen baseline data and the uniaxial yield surface are also shown. The determination and use of the local stress ratio in favor of the applied stress ratio may aid in the understanding and prediction of HCF behavior of notched components where stress redistribution occurs due to plasticity.

The concept of a critical distance from the notch root over which the stresses may be averaged is under investigation. The distance over which the average stress range in the axial direction of a notched specimen is equal to that of a smooth specimen for fatigue lives of  $10^6$  cycles, calculated from elastic-plastic FEM solutions, is plotted versus the averaged mean stress in Figure 7. Plotting the critical distance on a log scale, it may be possible to draw a straight line through the data points, and to develop a scheme for predicting the fatigue life of a notched component based upon a combination of FEM stress solutions and empirical data. With this definition of a critical distance, it is presently clear that there is a trend for the critical distance to increase with increasing stress ratio and mean stress. However, the scatter in the limited data available for the different notch geometries mandates that predictions must be regarded as rough estimates. The use of the von Mises effective stress and maximum shear stress, as well as various weighting factors, have led to essentially the same results. Attempts at using these data for the prediction of the loading conditions for fatigue lives of  $10^6$  cycles is planned for notched specimens having different  $K_t$ .

The interaction of initial LCF loading upon the HCF fatigue limit of notched specimens is also under investigation. The stress amplitude resulting in a fatigue life of 10,000 cycles, for  $R = 0.1$  at a frequency of 1 Hz, has been estimated from stress-life data for the notched cylindrical specimens. The HCF fatigue limit for notched specimens with 10, 1000, or 2500 initial LCF cycles, corresponding to 0.1, 10, and 25 percent of the 10,000 fatigue cycle life, has been found using the step loading method. Figure 8 shows the HCF fatigue limit at  $R = 0.1$ , for specimens with large circumferential notches subjected to an initial 1000 LCF cycles. Baseline HCF fatigue limits, with no initial LCF loading cycles, are also provided. Figure 8 shows that the  $10^6$  cycle fatigue limit actually improved after the application of 1000 LCF cycles. This may be due to plasticity-induced stress

redistribution, which effectively reduces both the maximum stress and local stress ratio at the notch root during subsequent HCF loading from those present during baseline fatigue limit testing.

Figure 9 provides more extensive results, where the HCF loading has been performed at  $R = 0.8$ . Results for both notch sizes are included, for initial LCF loadings of 10, 1000, and 2500 cycles. Baseline results for the HCF fatigue limit at  $R = 0.8$  with no LCF damage are also shown. Results for specimens with 10 initial LCF cycles fall within the scatter of the baseline HCF data. Since additional stress redistribution is occurring during the first cycle of the HCF loading after LCF loading, the maximum stress at the notch tip is not affected by the preceding LCF loading. Therefore, an increase in the HCF fatigue limit should not be expected. It should be noted that time-dependent stress redistribution has not yet been considered in any of these analyses.

It may be stated that no significant detrimental damage is occurring during the initial LCF loading for up to 25 percent of LCF life with the small notch and 10 percent of LCF life for the large notch. There appears to be a dip in the maximum stress for the small notch data at 1000 LCF cycles. It is possible that there is merely a wide scatter band in the fatigue limit for the small notch. Additional tests are planned to verify and extend these results.

This material is based upon work supported by the U.S. Air Force National Turbine Engine High Cycle Fatigue (HCF) Program.

Lanning, D., Haritos, G. K. and Nicholas, T., 1999, "Notch Size Effects in HCF Behavior of Ti-6Al-4V," to appear in *International Journal of Fatigue*.

Leven, M. M., 1955, "Stress Gradients in Grooved Bars and Shafts," *Proc. Society Experimental Stress Analysis*, Vol. 13, No. 1, pp. 207-213.

Maxwell, D. C. and Nicholas, T., "A Rapid Method for Generation of a Haigh Diagram for High Cycle Fatigue," *Fatigue and Fracture Mechanics: 29th Volume*, ASTM STP 1321, T. L. Panontin and S. D. Sheppard, Eds., American Society for Testing and Materials, 1998, (in press).

Nisitani, H. and Noda, N., 1984, "Stress Concentration of a Cylindrical Bar With a V-Shaped Circumferential Groove Under Torsion, Tension or Bending," *Engineering Fracture Mechanics*, Vol. 20, No. 5/6, pp. 743-766.

Peterson, R. E., 1974, **Stress Concentration Factors**, John Wiley and Sons, New York.

**Table 1.** Mechanical properties of the Ti-6Al-4V plate forging

PROPERTY / STRAIN RATE	0.0005 s <sup>-1</sup>	0.05 s <sup>-1</sup>
Yield Stress (MPa)	930	1003
Ultimate Stress (MPa)	979	1014
Elastic Modulus (GPa)	119	127

**Table 2.** Dimensions for flat double-notched specimens, with a notch angle of 60° and  $K_t = 2.72$ 

	SMALL NOTCH	LARGE NOTCH
$W$ (mm)	5.51	5.51
$h$ (mm)	0.131	0.635
$r$ (mm)	0.152	0.432
$t$ (mm)	1.524	1.524

**Table 3.** Dimensions for circumferential V-notch sizes, with a notch angle of 60° and  $K_t = 2.78$ 

	SMALL NOTCH	MEDIUM NOTCH	LARGE NOTCH
$D$ (mm)	5.72	5.72	5.72
$h$ (mm)	0.127	0.254	0.729
$r$ (mm)	0.127	0.203	0.330
$d$ (mm)	5.47	5.21	4.26

**Table 4.** Fatigue notch factors for cylindrical and flat dogbone Ti-6Al-4V specimens

NOTCH SIZE	$K_f$ ( $R = 0.1$ )	$K_f$ ( $R = 0.5$ )	$K_f$ ( $R = 0.8$ )
Large, cylindrical	2.16	1.86	1.24

Medium, cylindrical	2.05	1.89	1.27
Small, cylindrical	2.20	1.79	1.26
Large, flat	2.70	2.19	1.30
Small, flat	2.25	1.84	1.12

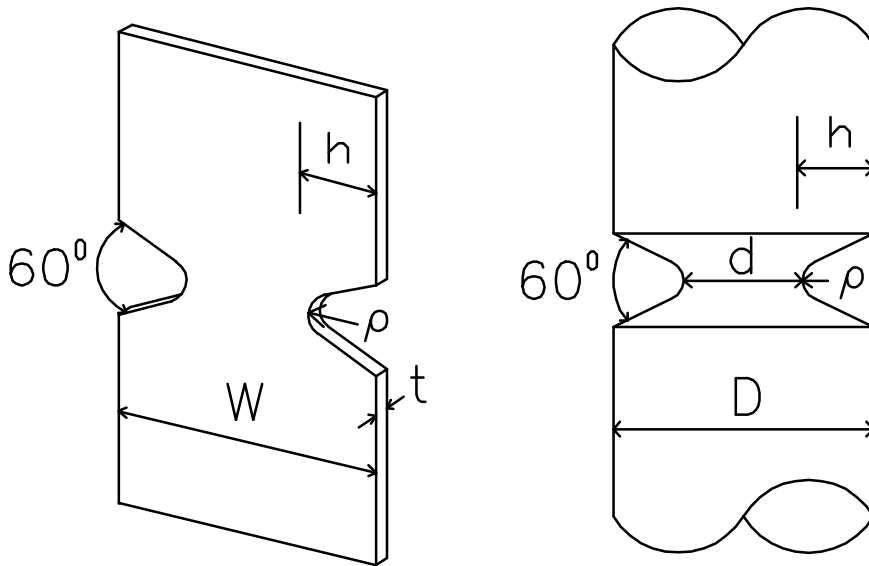


**Figure 1.** Gage sections of the flat dogbone and cylindrical fatigue specimens with V-notches.

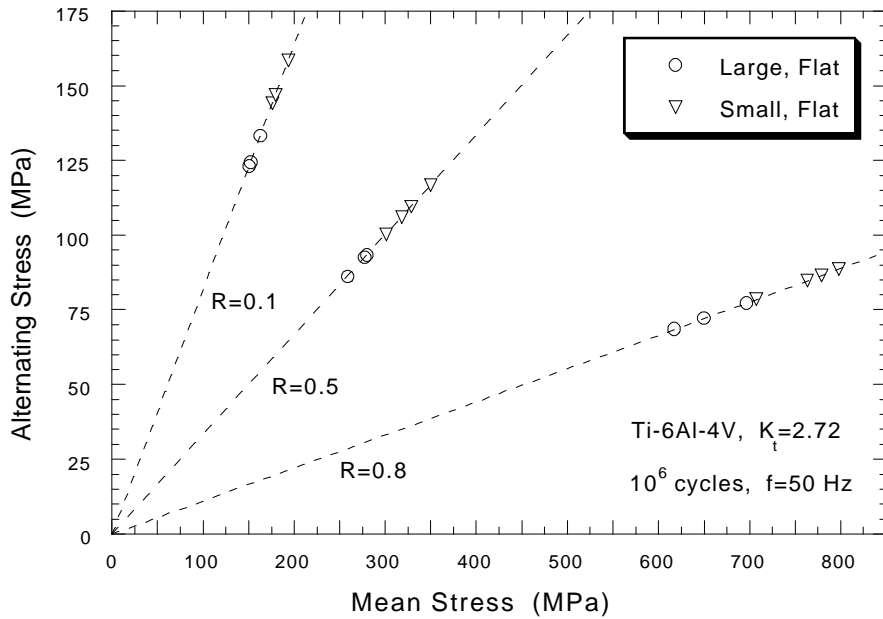


**Figure 2.** Constant life ( $10^6$  cycles) Haigh diagram for notched flat dogbone Ti-6Al-4V specimens.

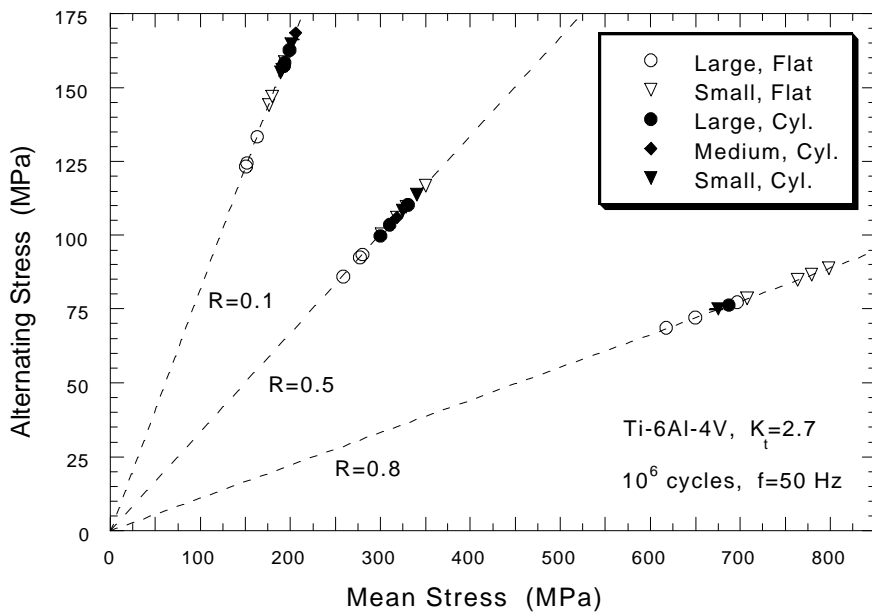


**Figure 3.** Constant life ( $10^6$  cycles) Haigh diagram for both flat and cylindrical Ti-6Al-4V specimens.



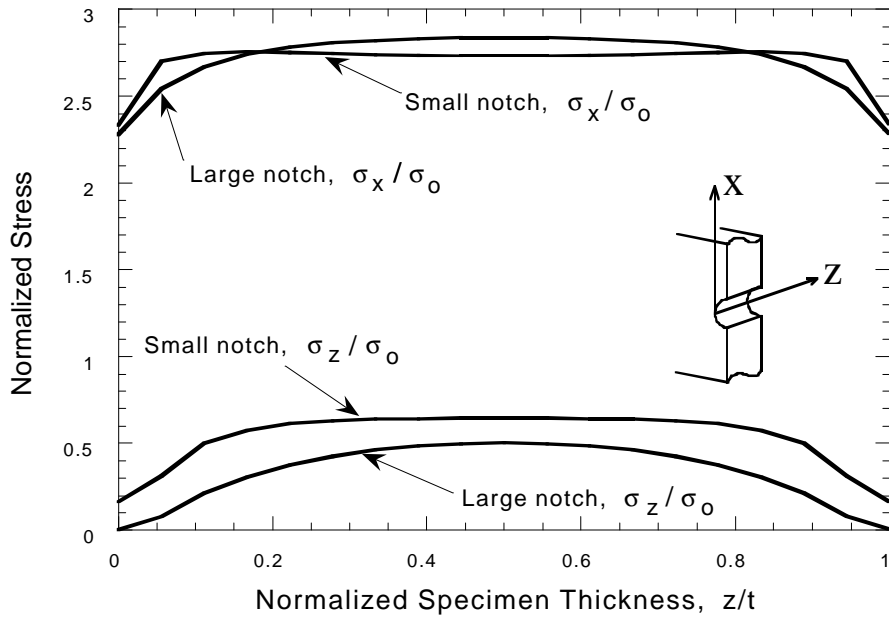


**Figure 4.** Normalized stress distribution in the thickness direction along the notch root of dogbone fatigue specimens. Specimen thickness is 1.524 mm and  $S_o$  is the average stress across the reduced section.

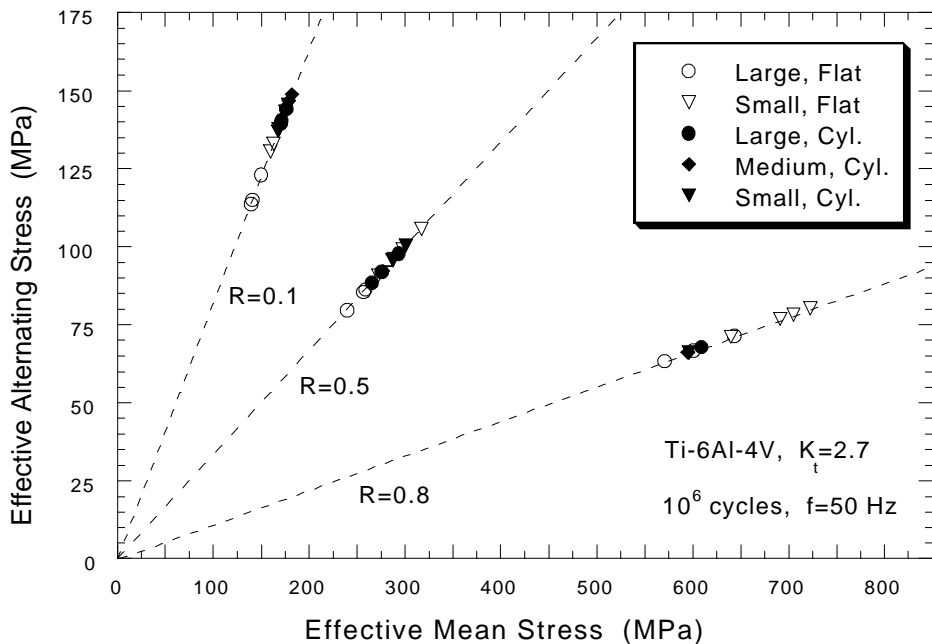


**Figure 5.** Constant life ( $10^6$  cycles) Haigh diagram for both dogbone and cylindrical notched Ti-6Al-4V specimens in terms of von Mises effective stresses.

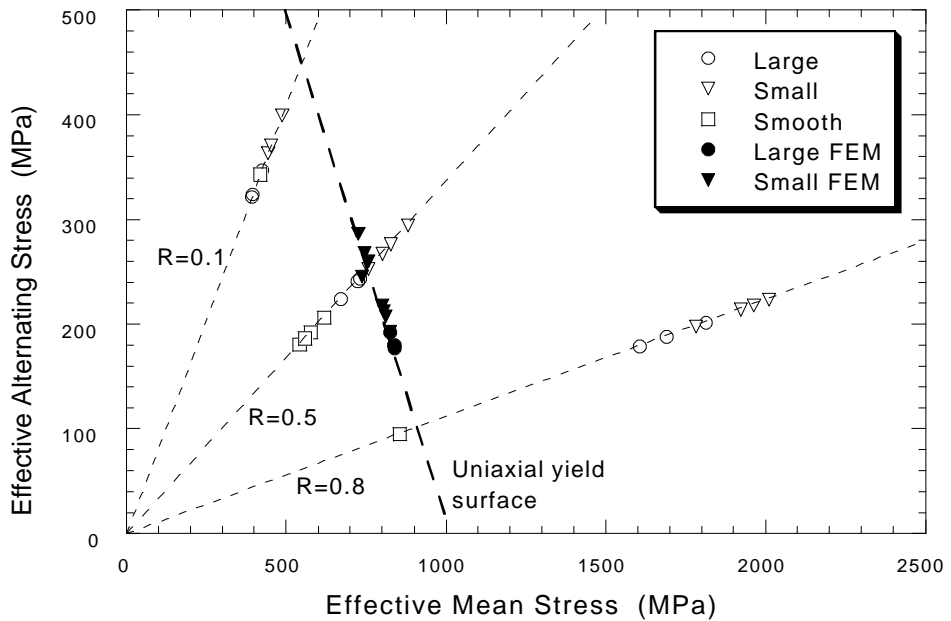


**Figure 6.** Constant life ( $10^6$  cycles) Haigh diagram for notched flat dogbone Ti-6Al-4V specimens. Solid data points represent FEM results for mean and alternating effective stresses at the notch root after stress redistribution.

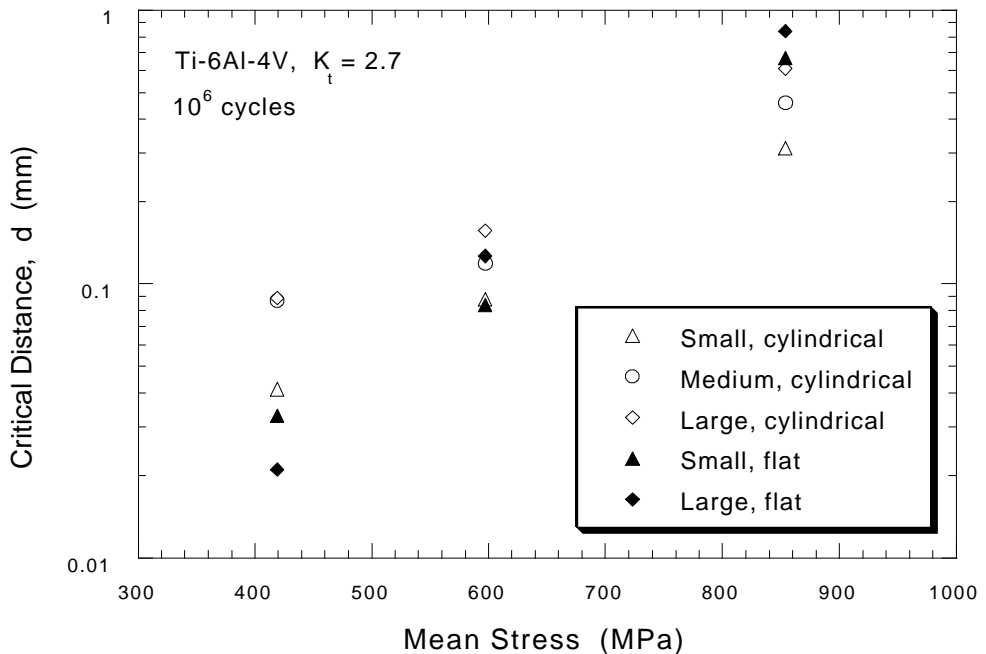


**Figure 7.** Critical distance from notch root versus mean stress.

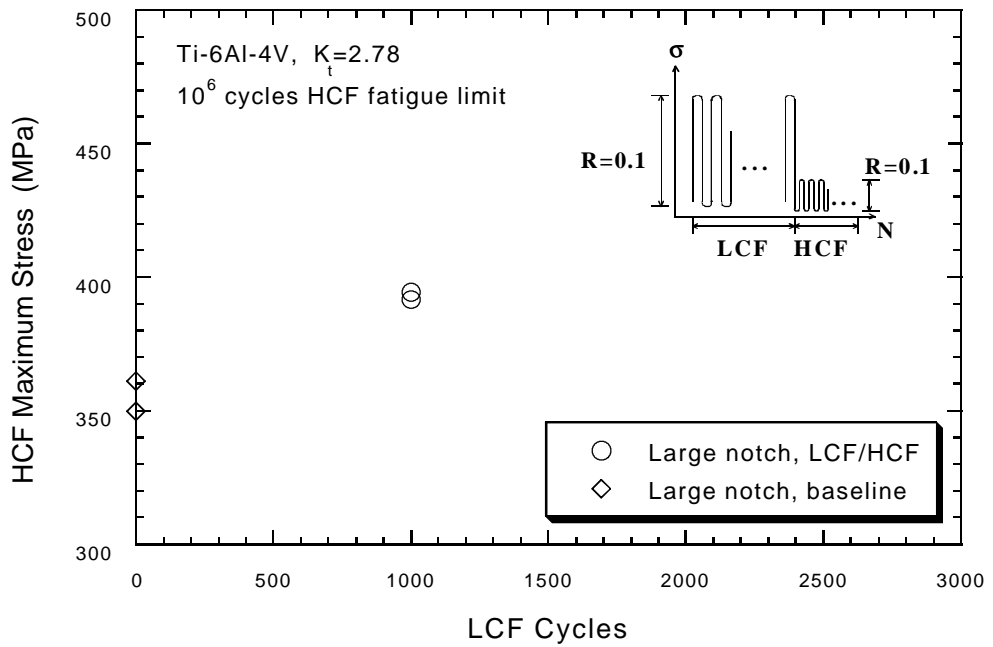


**Figure 8.** Maximum stress of HCF fatigue limit versus number of initial LCF loading cycles.

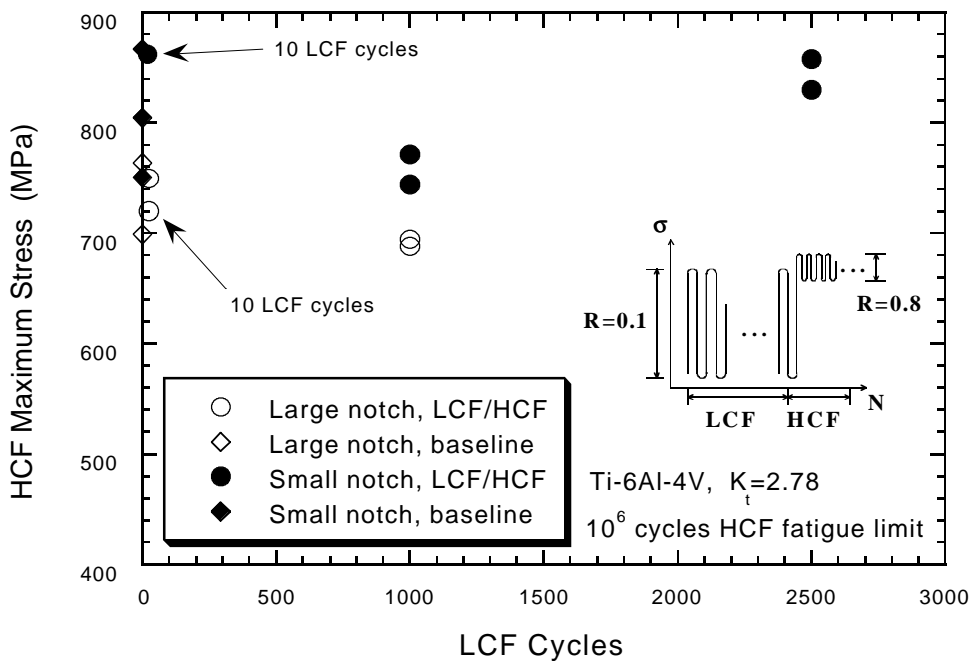


**Figure 9.** Maximum stress of HCF fatigue limit versus number of initial LCF loading cycles.

Department of Materials Science and Mineral Engineering  
University of California at Berkeley

---

## MEASUREMENT OF RESIDUAL STRESSES IN IMPACT-DAMAGED Ti-6Al-4V

---

**B.L. Boyce<sup>\*</sup>, A.W. Thompson, O. Roder, and R.O. Ritchie**

Department of Materials Science and Mineral Engineering  
University of California, Berkeley, CA 94720-1760

to be presented at the  
*4<sup>th</sup> National Turbine Engine High Cycle Fatigue Conference*  
Monterey, California, Feb.1999

February 1999

Work supported by the U.S. Air Force Office of Scientific Research under Grant No. F49620-96-1-0478 under the auspices of the Multidisciplinary University Research Initiative on *High Cycle Fatigue* to the University of California. The use of the Advanced Light Source and Stanford Synchrotron Radiation Laboratory is supported by a Laboratory Director's Research and Development fund from Lawrence Berkeley National Laboratory funded by the U. S. Department of Energy under contract #DE-AC03-76SF00098.

# MEASUREMENT OF RESIDUAL STRESSES IN IMPACT-DAMAGED Ti-6Al-4V

**B.L. Boyce<sup>\*</sup>, A.W. Thompson, O. Roder, and R.O. Ritchie**

Department of Materials Science and Mineral Engineering  
University of California, Berkeley, CA 94720-1760

**Abstract** - Residual stresses have long been difficult to measure with adequate resolution or accuracy on the appropriate scale, which is usually microstructural in size. However, availability of bright X-ray sources from particle accelerators, such as the Advanced Light Source at Lawrence Berkeley National Laboratory, may change this situation. Several orders of magnitude brighter than conventional X-ray beams and with excellent parallelism, accelerator sources can provide sufficient intensity to make very small beam sizes practical, thus permitting spatial resolution focused to a beam size of  $\sim 1 \mu\text{m}^2$ . One technique under consideration is the use of white light in micrometer beam sizes, which permits interrogation of an individual grain to determine orientation, followed by use of a monochromatic beam to measure six reflections and deduce the full stress state of that grain.

## RESIDUAL STRESSES AROUND IMPACT SITES AND INDENTS

Foreign objects ingested by turbine engines during operation can cause significant damage to fan and/or compressor airfoils. Under the influence of high cycle fatigue, these damage sites can lead to crack formation and propagation thereby degrading component lifetime [1-5]. For this reason, Foreign Object Damage (FOD) is a major concern of the HCF community. Perhaps one of the biggest challenges in the prevention of FOD-related failures lies in understanding the nature of the damage caused by the FOD impact. A better understanding of this damage would provide valuable insight into the formation and propagation of FOD-initiated fatigue cracks allowing a more realistic lifetime estimate.

The nature of the residual stresses around a surface damage site has been predominantly studied by two communities: (1) those interested in the residual stresses associated with hardness indents for measuring either resistance to cracking or prior residual stress [6-8] and (2) those interested in the residual stress field formed from the shot peening process [9-14]. Literature related to stresses around hardness indents has almost exclusively focused on the problem of the sharp indenter, which is most commonly used for estimates of cracking resistance or prior residual stress. While the analysis of the sharp indenter problem is relevant in its reliance on determining elastic-plastic response, the quasi-static velocities and non-axisymmetric geometry limit its applicability to the FOD case.

The shot peening residual stress literature, although much less extensive, has focused on the spherical impact problem where both the shape and velocity of the impact are more similar to the FOD problem. The experimental or theoretical quantification of residual stresses around an indent is quite complex due to the large number of variables involved. However, the most important initial parameters include: indenter and specimen material (including knowledge of modulus, yield strength, and work hardening parameters), indenter size, and impact velocity (or force in the case of quasi-static indentation), Figure 1. The easiest resultant variables to analyze include crater diameter and crater depth as well as surface residual stresses (typically by x-ray diffraction). A partial list of round-indenter literature as well as the parameters analyzed is presented in Table 1. A few of the experimental and theoretical results from these studies are shown in Figure 2 for the variation of stress in the Z direction (directly down from the indent, perpendicular to the surface), in Figure 3 for the variation of stress in the X direction (under the indent, parallel to the surface), and in Figure 4 for the variation of stress on the surface outside of the crater rim.

**Table 1.** Summary of selected studies on the residual stresses caused by a round indenter.

Investigators	Year	Type of Study	Material	Static or Dynamic	Velocity (m/s)	Indenter Dia. (mm)	Crater Dia. (mm)	Crater Depth ( $\mu\text{m}$ )	Stresses in Direction			Comments
									Surface	Bottom X	Bottom Z	
Kobayashi, Matsui, Murakami	1998	Experimental (X-ray)	Steel (HRC61) on steel	Both	6.3 m/s	50, 76	7	180-200	X Y			The effect of secondary impacts on a primary residual stress field
Al-Obaid	1990	Theoretical	Steel on steel	Dynamic	37-91 m/s	0.36		18-200			X	Dynamical considerations estimate crater depth and plastic zone size
Yokouchi, Chou, Greenfield	1983	FEM	Rigid on copper	Static		1.5	0.12			X Y Z	X Y Z	An attempt to correlate to the dynamic case (~0.2 m/s)
Li, Yao Mei, Duo, Renzhi	1991	Theoretical + Experimental (X-ray)	40Cr Steel on 40Cr Steel	Dynamic (multiple shots)	140N-320N*	1.1, 0.55					X Y	Comparison of predicted and mesured residual stresses on a peened surface
Studman and Field	1977	Theoretical + Experimental (Cracking)	WC on EN44B carbon steel (800 DPN)	Static	250N/s	10	1.7-2		X Y			Radial and circumferential stresses correlated to cracks formed at rim of indent
Peters and Roder	1998	Experimental	Cr-hardened steel on Ti-6Al-4V	Dynamic	100-300 m/s	3.2	1.5-2.5	100-300				MURI FOD Simulation

\* Velocity described by the static force (in N) to cause an equivalent crater size.

CURRENT AND POTENTIAL TECHNIQUES FOR MEASURING RESIDUAL STRESS

There are several techniques that are widely used for the measurement of residual stresses. A partial list of these techniques as well as some of the features of each technique are described in Table 2.

Table 2. Some of the more common techniques for measuring strain or residual stress.

Technique	Example References	Resolution			Stress Dimensionality	Nondestructive?	Other Restrictions?
		~1 μm	~100 μm	~1 mm			
X-ray Diffraction	Prevey [15] Cullity [16]			✓	3	✓	
SEM strain mapping	Davidson [17] Tong [18]	✓			2	✓	Strain grid or DIC
Indentation	Suresh and Giannakopoulos [6]	*	✓		1		
Hole Drilling	Beghini and Bertini [19]			✓	2		
Moire Interferometry	Wang and Chiang [20] Nishioka <i>et al.</i> [21]	✓			2	✓	Ridged surface
Raman Spectroscopy	Muraki, <i>et al.</i> [22]	✓			1	✓	Ceramic

\*Nanoindentation techniques have been used for achieving ~1 micron spatial resolution [6].

There are a handful of additional techniques which are not included in Table 2 including layer removal/curvature techniques, neutron diffraction and piezospectroscopy. Of the techniques listed in Table 2, only x-ray diffraction is readily capable of measuring the 3-dimensional residual stress state. Typical lab x-ray diffraction, however, is limited in spatial resolution to ~1 mm. However, synchrotron microdiffraction may be able to provide a nondestructure probe of ~1-10 μm resolution capable of determining the full 3-D stress-tensor, with variable depth penetration (as controlled by incident energy).

SPATIALLY RESOLVED RESIDUAL STRESS MEASUREMENTS USING SYNCHROTRON DIFFRACTION

Unlike typical lab diffractometers, synchrotron radiation provides a very bright, highly collimated, focusable beam of x-rays, which by virtue of the parallel beam can be highly monochromatic. The monochromatic beam allows for a very accurate analysis of peak position thereby providing strain resolution typically ~10<sup>-5</sup>. The Advanced Light Source (ALS) is currently in the process of developing a station for microdiffraction experiments capable of producing a 0.8 by 1.5 μm spot size with a photon flux of 10<sup>9</sup> ph/sec in a 1 eV bandpass at 10 keV. In this setup, both white light and monochromatic light (tunable from 4 to 12 keV) can be used interchangeably without moving focus. The experimental setup is shown in Figure 5.

The most common method for using x-ray diffraction to obtain residual stress information is the sin<sup>2</sup>ψ technique, Figure 6. In this technique, a tensile strain is deduced by comparing the d-

spacing of planes parallel to the specimen surface,  $d_n$ , and planes tilted at some angle,  $\psi$ , from the surface normal,  $d_i$ . The strains in the two directions are compared using elasticity theory:

$$\epsilon_\psi - \epsilon_n = \frac{\sigma_\phi}{E} (1 + \nu) \sin^2 \psi$$

From this, the stress can be determined from the difference in d-spacings:

$$\sigma_\phi = \frac{E}{(1 + \nu) \sin^2 \psi} \left( \frac{d_i - d_n}{d_n} \right)$$

Typically this analysis is performed on an aggregate of grains so that there are a sufficient number of grains oriented properly for angular integration. The  $\sin^2 \psi$  method requires a sufficient number of randomly oriented grains to be interrogated to get adequate angular integration, which in turn requires large beam dimensions. This method is thus most useful for wider gradients or larger sources of residual stress (e.g. large indents).

When, as in the case of FOD, the spatial scale of interest is smaller than several grains, strain information can be obtained from individual grains. Using synchrotron irradiation, white light can be focused on a single grain to deduce orientation. With orientation of the crystal known, a monochromator is moved into the beam without changing focus. The monochromator is tunable from 4 to 12 KeV, allowing the measurement of precise energy of an indexed reflection. The difference in d-spacing between the strained and unstrained case provides an absolute measurement of strain, and by measuring six reflections, the complete stress state for an arbitrary strain field can be determined. Moreover, it is possible to tune the photon energy to control the penetration depth from which the strain information is extracted (for example, see [23]).

While the facility for microdiffraction at the Advanced Light Source is in its final stages of preparation, preliminary studies have been performed at the Stanford Synchrotron Radiation Laboratory on beamline 2-1. A dogbone tensile specimen with a rectangular cross-section was machined out of Ti-6Al-4V in the solution treated and overaged (STOA) condition. The flat plane of the dogbone specimen was normal to the T-forging direction. The STOA microstructure consisted of a bimodal distribution of lamellar  $\alpha + \beta$  in a matrix of 64.1 $\pm$ 6.6 vol% primary- $\alpha$ . The 2 $\theta$  diffraction pattern collected at 10 keV on an unstrained dogbone specimen is shown in Figure 7 with the peaks from both the HCP  $\alpha$  phase and the BCC  $\beta$  phase labeled. The dogbone specimens were loaded in an *in-situ* strain rig capable of applying a fixed strain during x-ray analysis. Several peaks were interrogated at each of 10 applied strain levels ranging from the 0 to 6x10<sup>-3</sup>. The peak shift corresponding to the (10-10) peak at 5 applied strain levels is shown in Figure 8. From the 2 $\theta$ -intensity data, a lorentzian distribution was fitted to each peak and the center of the lorentzian fit was taken as the peak position. That peak position was then converted into a d-spacing and compared to the unstrained d-spacing to evaluate the measured strain. All data was collected in the “standard” x-ray diffraction mode where the bisector of the incident and diffracted beam was normal to the specimen surface. Thus, all crystallographic planes analyzed were coincident with the plane of the dogbone specimen and measured d-spacings corresponded to the Poisson contraction response to the applied strain. The comparison of measured strain to applied strain for both the (0002) and (10-10) peaks is shown in Figure 9. There is up to ~3x10<sup>-4</sup> error in estimating the applied strain which corresponds to a 1x10<sup>-4</sup> error in the actual measurement (due to the Poisson’s ratio between measured and applied strain). The accuracy of the strain measurement could be improved by (a) measuring at higher 2 $\theta$  angles



where the  $2\theta$  position is more sensitive to d-spacing<sup>1</sup>, (b) increasing the count time to improve statistics, or (c) using a more accurate fit routine to determine the centroid of the peak.

While the accuracy of the strain measurement is one concern, there are several other issues which must be addressed before this technique will be useful for investigating the residual stresses around foreign object damage. These issues include (a) proper control of the specimen temperature to avoid thermal strain, (b) a micropositioning technique for aligning the beam on the specimen, (c) CCD processing techniques to deduce single crystal orientation when several grains are present, (d) a method to control penetration depth with incident energy (e) the verification of currently available elastic constants used to convert the measured strain to stress, and (f) if sectioning is used to expose cross-sections, an analysis of the redistribution of stresses

## SUMMARY

Understanding the nature of the residual stress distribution around the site of foreign object damage is critical to addressing the issue of FOD-related failures under HCF. While indentation literature primarily focuses on the sharp indenter problem, there have been several theoretical and experimental studies on the problem of the round indenter under both static and dynamic conditions that will form the basis for further work. Although there are several techniques available for the measurement of residual stresses, no current technique is available for measuring the 3-D stress state in damaged metallic specimens at the resolution necessary to deduce stress gradients with a resolution of 1-100  $\mu\text{m}$ . For this reason, we are beginning to investigate the possibility of using focused synchrotron x-ray diffraction to measure residual stresses. The high brightness and highly collimated beam which is focusable down to a  $\sim 1\ \mu\text{m}$  spot size is ideal for this type of analysis. Preliminary studies indicate that strains in the range of  $10^{-5}$  will be detectable by this technique.

*Acknowledgments:* Supported by the Air Force Office of Scientific Research by the Multidisciplinary University Research Initiative on *High Cycle Fatigue* to the University of California under Grant No. F49620-96-1-0478. The use of the Advanced Light Source and Stanford Synchrotron Radiation Laboratory is supported by a Laboratory Director's Research and Development fund from Lawrence Berkeley National Laboratory funded by the U. S. Department of Energy under contract #DE-AC03-76SF00098. B.L.B. is supported by the Fannie and John Hertz Foundation.

---

<sup>1</sup> For example, the resolution in d-spacing would be improved by a factor of  $\sim 5$  at  $100^\circ\ 2\theta$  (the peak positions analyzed here were at  $\sim 30^\circ\ 2\theta$ ).

## REFERENCES

1. J. M. Larsen, B. D. Worth, C. G. Annis, Jr., and F. K. Haake, *Int. J. Fract.*, **80**, 237 (1996)
2. B. A. Cowles, "High cycle fatigue in gas turbines – an industry perspective," *Int. J. Fract.*, **80**, 147 (1996)
3. H. I. H. Saravanamutto, "Erosion, corrosion and foreign object damage in gas turbines," Technical Evaluator's Report, AGARD-CP-558, 1994, p. T.1.
4. F. Aydinmakine, "Understanding and preventing failures and their causes in gas turbine engines," *ibid.*, p. K.1.
5. C. DiMarco, "Navy foreign object damage and its impact on future gas turbine low pressure compression system," *ibid.*, p. G.1.
6. S. Suresh and A. E. Giannakopoulos, "A new method for estimating residual stress by instrumented sharp indentation," *Acta Mater.*, **46**, 5755 (1998)
7. J. Salomonson, K. Zeng, and D. Rowcliffe, "Decay of residual stress at indentation cracks during slow crack growth in soda-lime glass," *Acta Mater.*, **44**, 543 (1996)
8. K. Zeng, A. E. Giannakopoulos, D. Rowcliffe, and P. Meier, "Residual stress fields at the surface of sharp pyramid indentations," *J. Am. Ceramic Soc.*, **81**, 689 (1998)
9. M. Kobayashi, T. Matsui, and Y. Murakami, "Mechanism of creation of compressive residual stress by shot peening," *Int. J. Fatigue*, **20**, 351 (1998)
10. Y. F. Al-Obaid, "A rudimentary analysis of improving fatigue life of metals by shot peening," *J. App. Mech.*, **57**, 307 (1990)
11. Y. Yokouchi, T. W. Chou, and I. G. Greenfield, "Elastic-plastic analysis of indentation damages in copper: work hardening and residual stress," *Met. Trans. A*, **14A**, 2415 (1983)
12. Y. K. Li, Y. Mei, W. Duo, and W. Renzhi, "Mechanical approach to the residual stress field induced by shot peening," *Mat. Sci. and Eng.*, **A147**, 167 (1991)
13. C. J. Studman and J. E. Field, "The indentation of hard metals: the role of residual stresses," *J. Mater. Science*, **12**, 215 (1977)
14. K. L. Johnson, in *Engineering Plasticity*, Cambridge University Press, 341 (1968)
15. P. S. Prevey, "A method of determining the elastic properties of alloys in selected crystallographic directions for x-ray diffraction residual stress measurement," *Adv. X-Ray Anal.*, **20**, 345 (1977)
16. B. D. Cullity, *Elements of X-ray diffraction*, Second Edition, Addison-Wesley Publishing Company, Menlo Park, CA, 447 (1978)
17. D. L. Davidson, "Damage mechanisms in high cycle fatigue," Southwest Research Institute, July 1998.
18. W. Tong, "Detection of plastic deformation patterns in a binary aluminum alloy," *Experimental Mech.*, **37**, 452 (1997)
19. M. Beghini and L. Bertini, "Recent advances in the hole drilling method for residual stress measurement," *J. Mat. Eng. and Performance*, **7**, 163 (1998)
20. Y. Y. Wang and F. P. Chiang, "Experimental study of three-dimensional residual stresses in rails by moire interferometry and dissecting methods," *Optics and Lasers in Engineering*, **27**, 89 (1991)
21. T. Nishioka, M. Nishi, T. Fujimoto, K. Sakakura, "Moire interferometry measurements of near-tip deformation in inhomogeneous elastic-plastic fracture specimens," *Int. J. Pressure Vessels and Piping*, **63**, 261 (1995)
22. N. Muraki, G. Katagiri, V. Sergo, G. Pezzotti, and T. Nishida, "Mapping of residual stresses around an indentation in  $\beta$ -Si<sub>3</sub>N<sub>4</sub> using Raman spectroscopy," *J. Mat. Sci.*, **20**, 5419 (1997)
23. M. Harting, "A seminumerical method to determine the depth profile of the three dimensional residual stress state with x-ray diffraction," *Acta Mater.*, **46**, 1427 (1998).

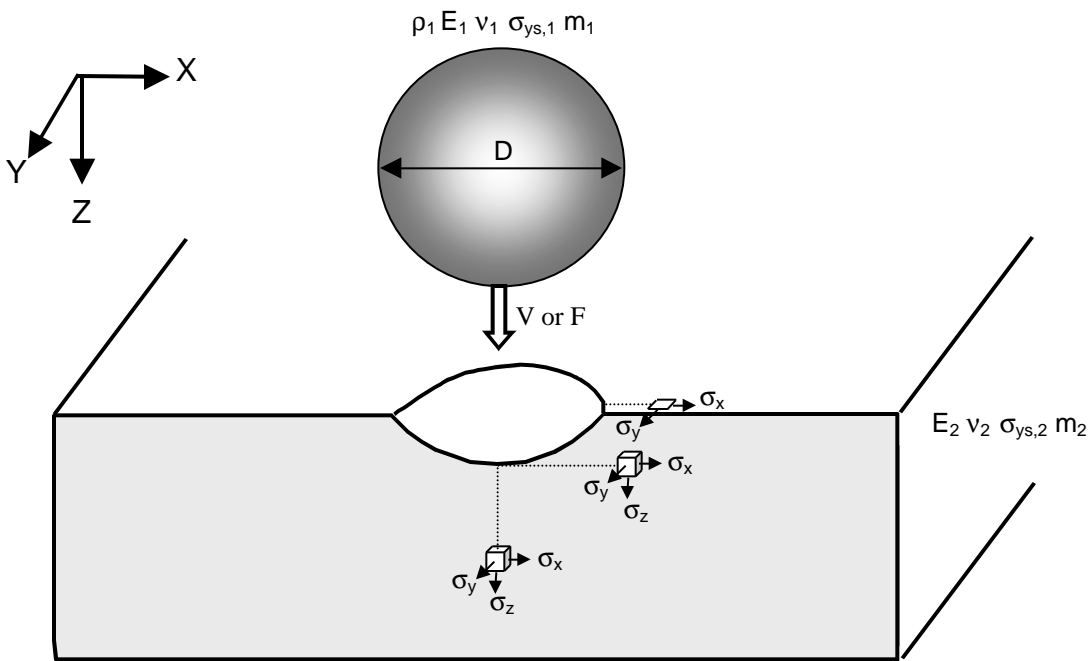


**Figure 1.** Some of the quantities involved in assessing the damage left around a spherical indent. The material properties of both the indenter and the specimen (elastic constants, yield strength, work hardening exponent) as well as the impact velocity (or force in the quasi-static case) and indenter diameter are typical input parameters. Output parameters include the crater depth and diameter as well as the 2-D stress state at the surface and the 3-D stresses directly below or to the side of the crater.

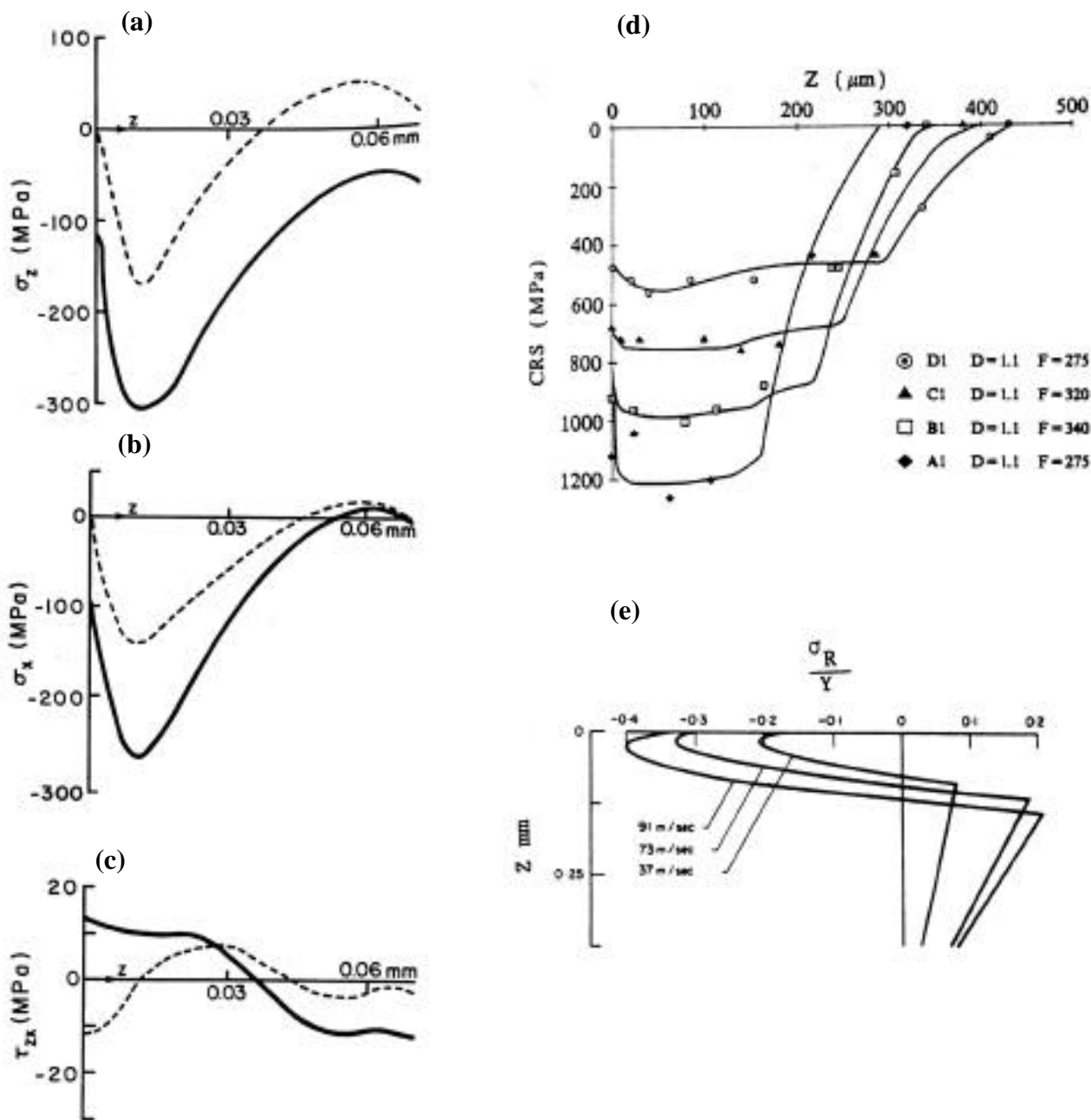


**Figure 2.** Variation of stress with depth ( $Z$ ) below the bottom of the indent. (a-c) FEM-determined values for  $\sigma_z$ ,  $\sigma_x$ , and  $\tau_{zx}$  at peak indenting load (solid) and after release (dashed), from [11], (d) theoretical (lines) and experimental (points)  $\sigma_x$  based on multiple shots (peened surface) using  $D=1.1\text{mm}$  shot at a force of 275-340 N, from [12], (e) theoretical  $\sigma_x$  (labeled  $\sigma_R$ ) for three shot velocities, from [10].

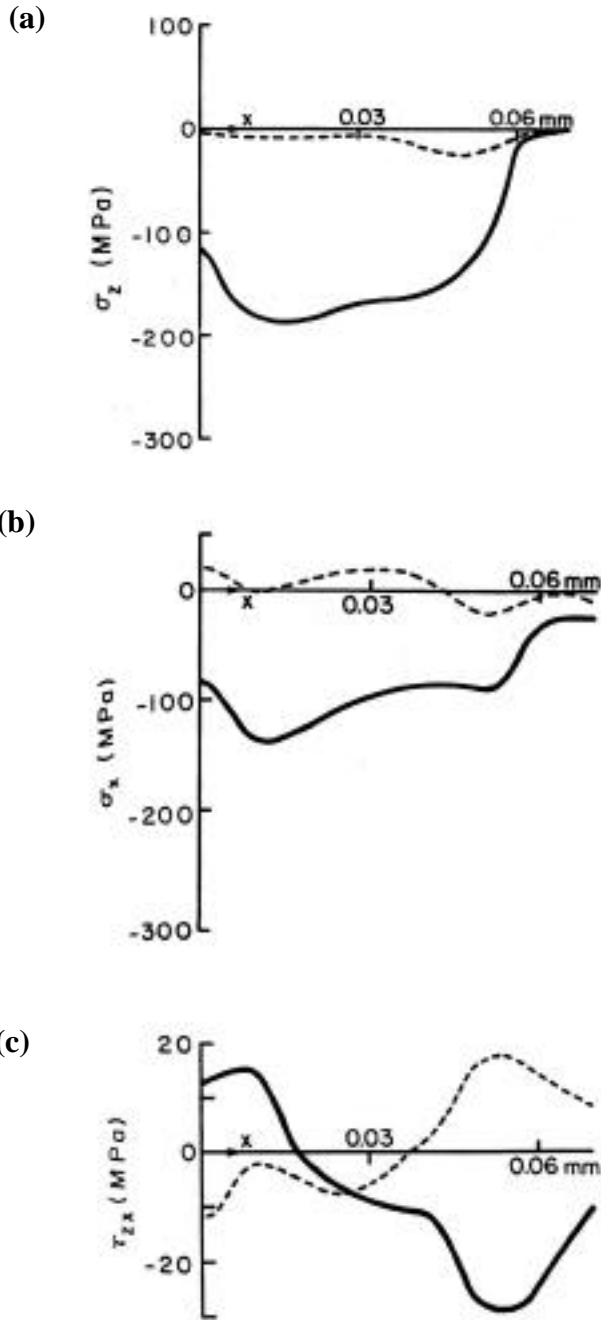


**Figure 3.** Variation of stress in the radial (X) direction from under the indent. (a-c) FEM-determined values for  $\sigma_z$ ,  $\sigma_x$ , and  $\tau_{zx}$  at peak indenting load (solid) and after release (dashed), from [11].

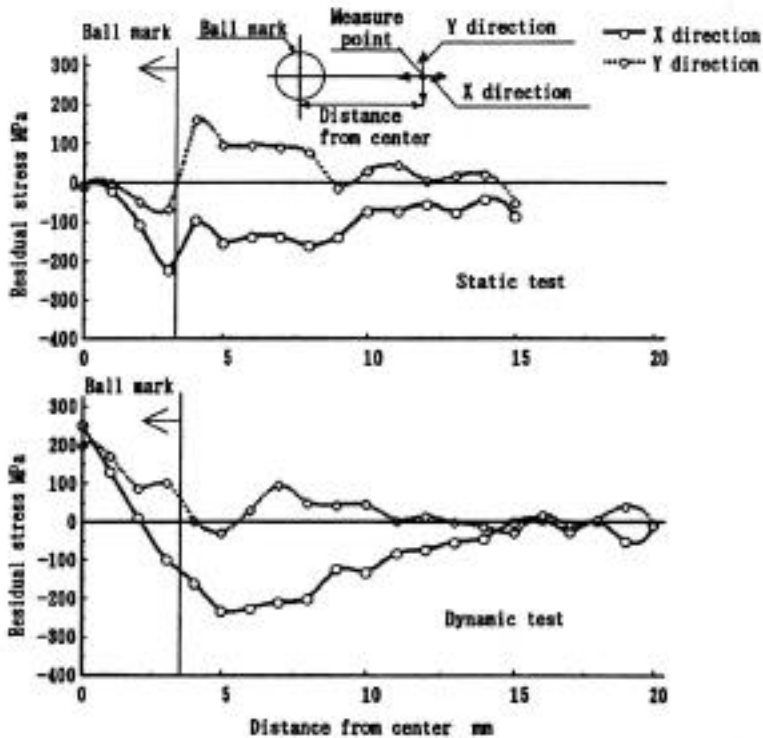


**Figure 4.** Variation of surface stress with distance from the crater rim. From [9].

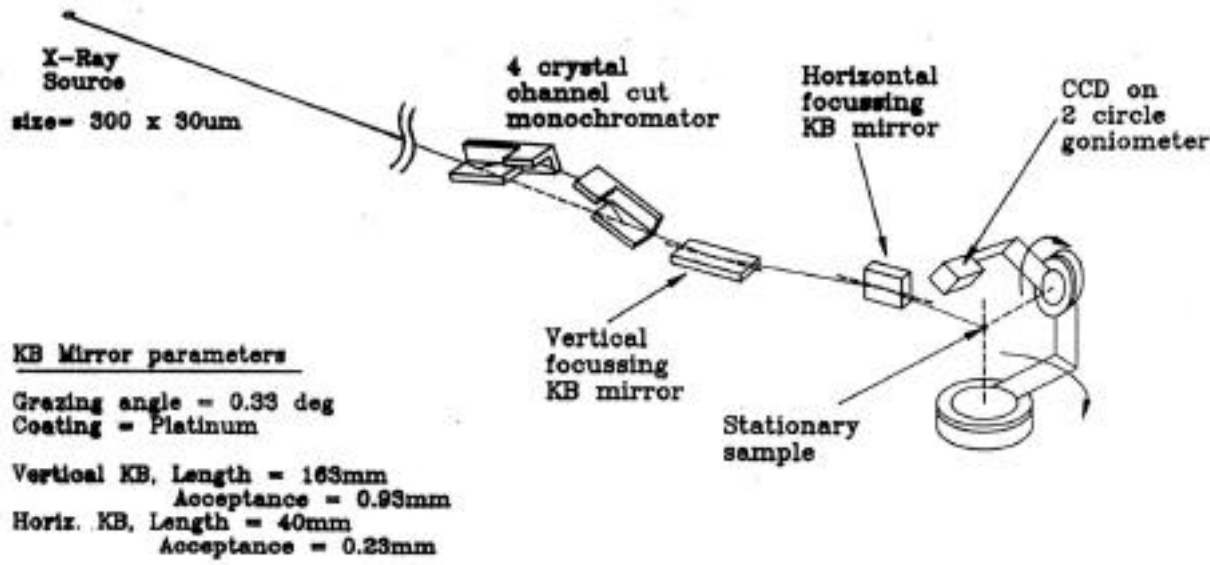
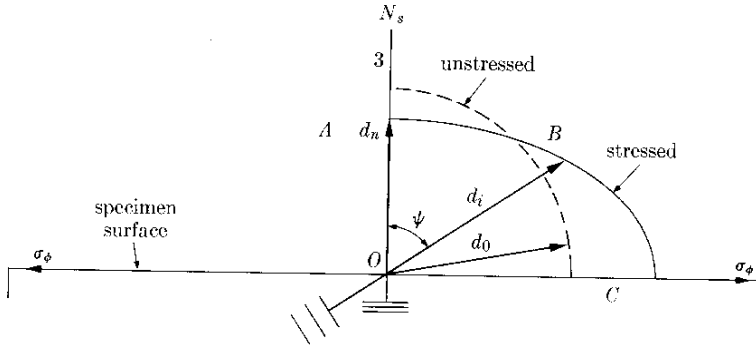


**Figure 5.** Microdiffraction setup at Advanced Light Source.



(a) Vector diagram of plane spacings  $d$  for a tensile stress  $\sigma_\phi$

**Figure 6.** The traditional  $\sin^2\psi$  technique as described in Cullity [16].

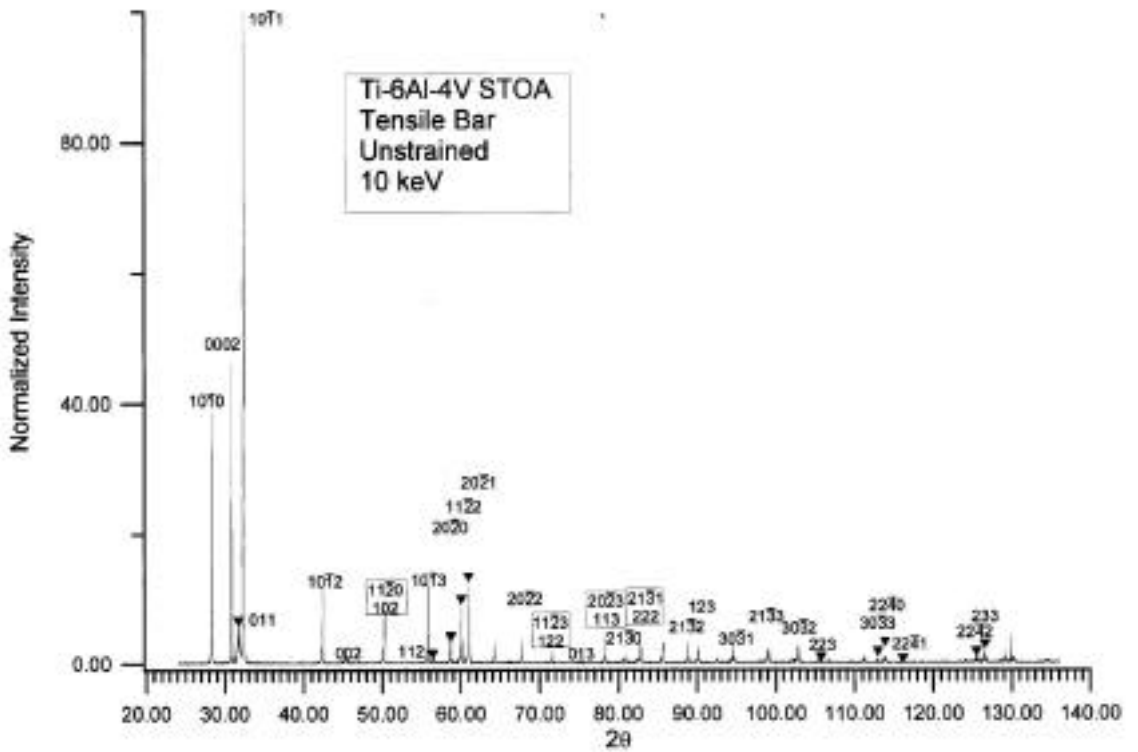


**Figure 7.**  $2\theta$  scan of Ti-6Al-4V in the unstrained condition at 10 keV. HCP- $\alpha$  peaks are labeled in 4-digit Miller-Bravais notation and BCC- $\beta$  peaks are labeled in 3-digit Miller notation. When the peaks from the  $\alpha$  and  $\beta$  peaks are indistinguishable, both indexes are noted with a box around them.

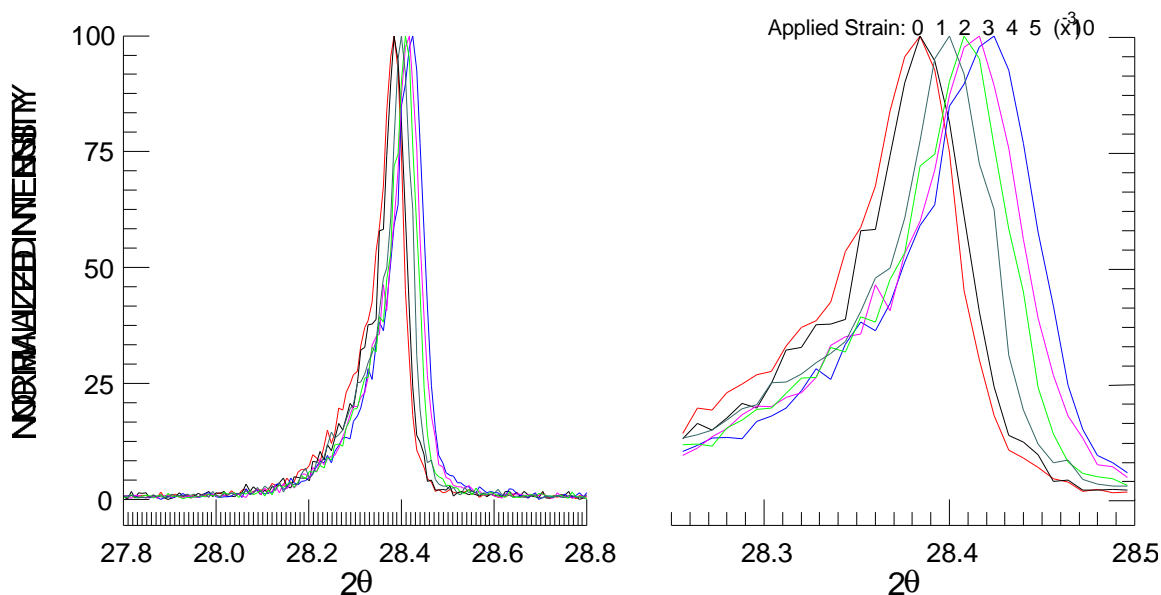


**Figure 8.** The (10-10) peak at 6 different strain levels ranging from 0 to  $5 \times 10^{-3}$ . The shift in peak position due to applied strain is apparent.

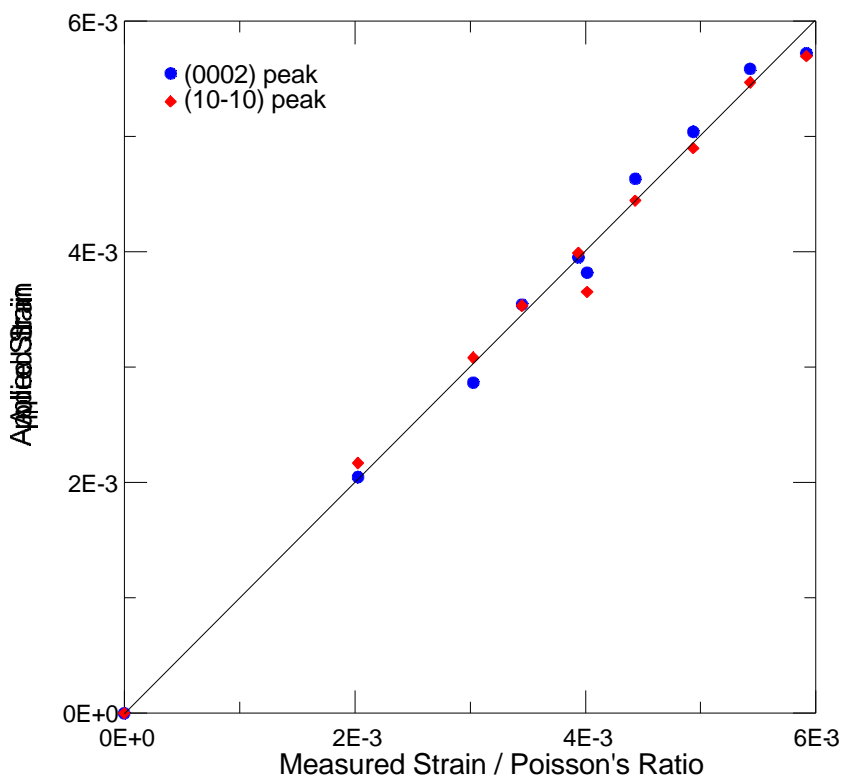


**Figure 9.** The (10-10) and (0002) peaks used to show the correlation between applied strain and measured strain. These peaks have been normalized by their respective Poisson's ratio, which are different due to the anisotropy of the  $\alpha$  phase.



# **INFLUENCE OF SIMULATED FOREIGN OBJECT DAMAGE ON THE HIGH-CYCLE FATIGUE PROPERTIES OF TI-6AL-4V FOR GAS TURBINE BLADES**

O. RODER, J. O. PETERS, A. W. THOMPSON, and R. O. RITCHIE

University of California at Berkeley  
Department of Materials Science and Mineral Engineering  
Berkeley, CA 94720-1760

## Introduction

The ingestion of foreign objects into jet engines powering military or civil aircraft can lead to severe structural damage of the fan and compressor airfoils; indeed, such foreign object damage (FOD) is a prime reason for maintenance and repair. In particular, the damage induced by small hard objects of millimeter size, in association with the typical load spectra experienced by airfoils, i.e., low-cycle fatigue (LCF) cycling due to normal start/flight/landing cycles superimposed with high-cycle fatigue (HCF) cycles due to vibrations and resonant loads, can lead to non-conservative life prediction and unexpected high-cycle fatigue failures. Specifically, the damage sites can provide initiation points for cracks, which then propagate under the HCF spectra of large numbers ( $>10^9$ ) of high frequency ( $>1$  kHz), high load-ratio ( $R \sim 0.8$ ) cycles. The objective of this study was to characterize (i) the size and shape of the indents and (ii) the level of microstructural damage induced by impacts of foreign objects, (iii) to examine the influence of foreign object damage on crack initiation and crack propagation that can lead to failure by HCF and (iii) how that crack propagation behavior is affected by microstructure. The primary study was performed on a fan/compressor blade processed (STOA) bi-modal microstructure of the titanium alloy Ti-6Al-4V. In addition, a  $\beta$ -annealed lamellar microstructure was investigated to isolate the role of microstructure.

## Material, Microstructures and Tensile Properties

The titanium Ti-6Al-4V alloy studied was delivered as a solution treated and overaged (STOA) forged plate. The plate came from a set of forgings produced specifically for the U.S. Air Force sponsored programs on HCF. Material and processing details are given in [1]. The plate material showed a bi-modal microstructure with a volume fraction of 60 % primary  $\alpha$  (diameter  $\sim 20$   $\mu\text{m}$ ) and 40 % lamellar  $\alpha+\beta$  matrix (Figure 1a). In addition to the bi-modal microstructure, a  $\beta$ -annealed lamellar microstructure (Figure 1b) was investigated for comparison. To obtain a lamellar microstructure, the delivered plate material was solution treated in the  $\beta$  phase field at 1005°C for 10 min. This  $\beta$ -annealing

resulted in large  $\beta$  grains with a diameter of approximately 1000  $\mu\text{m}$ . Controlled cooling with a rate of 100-130°C/ min to match the same lamellae width of the bi-modal microstructure (2  $\mu\text{m}$ ) resulted in a  $\alpha+\beta$  lamellae colony size of 500  $\mu\text{m}$ . Finally, to ensure comparability with the bi-modal microstructure, the lamellar microstructure was given the same final heat treatment step of 2 h at 705°C.

The uniaxial tensile properties of both bi-modal and lamellar microstructures are listed in Table 1:

Table 1: Tensile properties (strain rate  $5 \times 10^{-4} \text{ s}^{-1}$ )

Condition	$\sigma_{0.2}$ (MPa)	UTS (MPa)	El. (%)
Bi-modal [1]	930	970	20
Lamellar	975	1055	12

Simulation and Characterization of Foreign Object Damage

Foreign object damage by hard particles is simulated by firing chrome-hardened steel spheres on a flat specimen surface by using compressed gas to produce a single damage site. [2] The specimen geometry chosen for this study has a rectangular gauge section (3mm  $\times$  5mm) with cylindrical buttonhead grip sections (Figure 2). To provide a consistent, nominally stress-free surface, the gauge section was prepared by standard stress relief and chemical-milling procedures. In this study, spheres (diameter 3.175 mm) were impacted at an angle of 90° (normal impact) at velocities of ~200, 250 and 300 m/s. These velocities were chosen because (i) they represented typical in-service impact velocities on blades, and (ii) they provided different levels of damage (see below). Damage sites have been characterized to date in terms of the geometrical dimensions (shape, diameter, depth) and microstructural changes.

SEM micrographs of typical impact sites for the bi-modal microstructure are shown in Figure 3a (200 m/s) and Figure 3b (300 m/s). For the lamellar microstructure typical impact sites are shown in Figure 4a (200 m/s) and Figure 4b (250 m/s). For the bi-modal microstructure, corresponding cross sections of impact craters are shown in Figure 5a (200 m/s) and Figure 5b (300 m/s). While at 300 m/s (Figure 5b) and 250 m/s, tangential orientated shear bands (Figure 6) were seen emanating from the surface of the crater, such shear bands were not observed for 200 m/s impacts (Figure 5a). This result corresponds with the reported critical velocity of 214 +/-16 m/s to achieve shear bands in Ti-6Al-4V by an impacting 3.2 mm diameter steel sphere [4]. The amount and length of the observed shear bands increased with increasing impact velocity. In addition, the 300 m/s impacts caused a ridging along the crater rim (Figures 5b and 6b); this feature was not seen for the lower velocity impacts (Figure 5a). Figure 7 summarizes the relevant features in form of a schematic illustration of the crater profile. In the range of 100 to 320 m/s impact velocities, the diameter and depth of damage site increased linearly with increasing impact velocity.

## Influence of Foreign Object Damage on High-Cycle Fatigue

After impact, the tensile specimens were subsequently cycled at 20 Hz (sine wave) with a maximum nominal stress of 500 MPa at a load ratio of  $R = 0.1$ . Periodically, the specimens were removed from the test frame and examined in a scanning electron microscope (SEM) to detect crack initiation. Once a crack had initiated, subsequent crack growth was similarly monitored using periodic SEM observations. Stress intensities for the surface cracks were calculated from the Newman and Raju linear elastic solution for semi-elliptical surface cracks, assuming a half-surface length to depth ratio of 0.9 (determined from fractographic measurements). [3] In this initial study, contributions to the local stress intensity factor values from the geometry of the indentation and the residual stress field surrounding the indent have been ignored. Current studies are focused on the use of micro X-ray diffraction methods to measure such residual stresses.

The effect of the simulated foreign object damage was to markedly reduce the fatigue life compared to that obtained with an undamaged smooth-bar specimen [5], as shown in Figure 9 for the bi-modal microstructure. At maximum stresses of 500 MPa ( $R = 0.1$ ), surface cracks were initiated within  $\sim 3 \times 10^4$  to  $\sim 5 \times 10^4$  cycles, the failure of the impacted specimens occurred between  $\sim 4 \times 10^4$  and  $\sim 8 \times 10^4$  cycles. Specifically, fatigue lives were reduced by over two orders of magnitude following 200 m/s and 300 m/s impacts.

For the bi-modal microstructure, crack initiation sites of the small surface cracks are shown in Figure 10a (200 m/s) and in Figure 10b (300 m/s). First results show that the cracks tended to initiate at the bottom of the indent for the lower velocity impacts and at the crater rim for the higher velocity impacts. Corresponding fracture surfaces are shown in Figure 11a (200 m/s) and Figure 11b (300 m/s). The position of the crack front during crack extension is indicated schematically (Figure 11). For the 200 m/s impact, the initiation at the bottom of the indent can be explained by stress concentration due to the notch geometry. Crack initiation at the crater rim (300 m/s) might be related to circumferential residual tensile stresses at the crater ridge [e.g. 6], which overcompensate the stress concentration effect of the indent.

The presence of the tangential orientated shear bands do not appear to play a significant role in the initiation process of the fatigue cracks. This is thought to be due to the fact that at the center of the indent, the tangential aligned shear bands are parallel to the applied stress axis.

The growth of the small cracks originating from such impact sites are compared in Figure 12 with growth-rate data for large ( $>5$  mm) [7] and naturally-initiated small ( $\sim 45$ -1000  $\mu\text{m}$ ) [5] cracks for the bi-modal microstructure. Both the naturally-initiated and FOD-initiated small-crack velocities were within the same scatter band, initially up to an order of magnitude faster than corresponding large crack results. The small-crack data tended to merge with large-crack results above  $\Delta K = 10 \text{ MPa}\sqrt{\text{m}}$  as the crack size increased. However, in the limited data collected to date, no FOD-initiated cracks have been observed in the Ti-6Al-4V bi-modal microstructure below  $\Delta K = 2.9 \text{ MPa}\sqrt{\text{m}}$ ; i.e., no FOD-initiated cracking was observed below the worse-case (large crack) threshold,  $\Delta K_{\text{TH}}$  of  $1.9 \text{ MPa}\sqrt{\text{m}}$ , measured using constant  $K_{\text{max}}$  cycling at a final  $R$  ratio of 0.95 [7] Therefore, fatigue crack propagation thresholds of large cracks determined under

conditions that minimize crack closure can be used as a lower bound for the threshold stress intensities for FOD initiated cracks.

To examine the influence of microstructure in addition to the  $\alpha+\beta$  processed bi-modal microstructure, a  $\beta$ -annealed lamellar microstructure was also investigated. A typical crack initiation site of the small surface cracks is shown in Figure 13 for an impact velocity of 200 m/s. As shown previously for the bi-modal microstructure, cracks tended to initiate at the bottom of the indent for the 200 m/s and 250 m/s velocity impacts and that the presence of the tangential orientated shear bands did not appear to play a significant role in the initiation process. Further testing at higher velocities (300 m/s) is currently underway to evaluate crack initiation at the crater ridge.

Preliminary results of fatigue crack propagation tests of the lamellar microstructure are shown in Figure 14. It can be seen that the lamellar microstructure showed a slightly higher resistance against the propagation of small surface cracks as compared to the bi-modal microstructure. These preliminary results indicate that the resistance of the impacted microstructure against fatigue crack propagation is only minimally affected by significant changes in the microstructural dimensions (bi-modal vs. lamellar).

### Summary

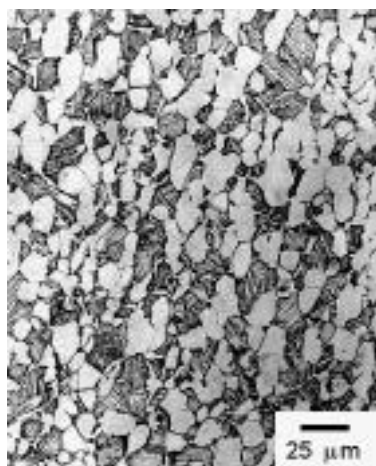
1. Foreign object damage, simulated by hardened steel spheres impacted at 200-300 m/s on a flat surface, provides sites for the initiation of small fatigue cracks.
2. At applied stresses some 10 % below the smooth-bar fatigue limit ( $10^7$  cycles), crack initiation lives were less than  $4 \times 10^4$  cycles, many orders of magnitude lower than lifetimes for un-impacted samples.
3. Subsequent propagation of small cracks from the damage sites was faster as compared to the propagation rates of large cracks subjected to the same applied  $\Delta K$  level.
4. No crack growth from the damage sites has been observed to date at  $\Delta K$  values less than  $2.9 \text{ MPa}\sqrt{\text{m}}$ . The “worse-case” large crack threshold value could thus be used as a lower bound to FOD initiated cracking.
5. Preliminary results of the microstructure comparison showed that the resistance against fatigue crack propagation was only minor affected by a drastic change of microstructure (bi-modal vs. lamellar).

### Acknowledgements

This work is supported by the Air Force Office of Science and Research, Grant No. F49620-96-1-0478, under the Multidisciplinary University Research Initiative on “High Cycle Fatigue” to the University of California, Berkeley.

## References

1. D. Eylon, "Summary of the Available Information on the Processing of the Ti-6Al-4V HCF/LCF Program Plates", University of Dayton Report, Dayton, OH. (1998).
2. R. O. Ritchie, S. Suresh, J. W. Hutchinson, W. W. Milligan, A. G. Evans, A. W. Thompson, "High-Cycle Fatigue and Time-Dependent Failure in Metallic Alloys For Propulsion Systems", AFOSR F49620-96-1-0478, Progress Report (1997).
3. J. C. Newman, Jr., and I. S. Raju, *Eng. Fract. Mech.* **15**, 185 (1981).
4. S. P. Timothy and I. M. Hutchings, in *Proceedings of the 3<sup>rd</sup> Conference on Mechanical Properties at High Rates of Strain*, The Institute of Physics, 1984, 397.5
5. J. A. Hines, J. O. Peters and G. Lütjering, "Microcrack Propagation in Ti-6Al-4V", in *Fatigue Behavior of Titanium Alloys*, R.R. Boyer, D. Eylon, J.P. Gallagher and G. Lütjering, TMS, Warrendale, PA, 1999.
6. C.J. Studman, J.E. Field, "The Indentation of Hard Metals: The Role of Residual Stresses", *J. Mater. Sci.* **12**, 215 (1977).
7. B. L. Boyce, J. P. Campbell, O. Roder, A. W. Thompson, W. W. Milligan, and R. O. Ritchie, *Int. J. Fatigue* (1999), accept for publication and in press.



a) Bi-modal



b) Lamellar

Fig. 1: Microstructures (LM)

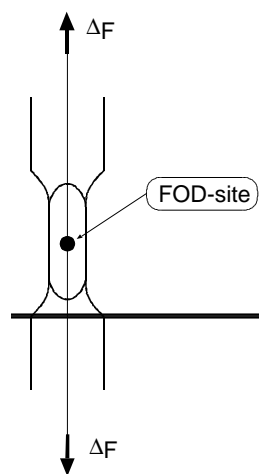
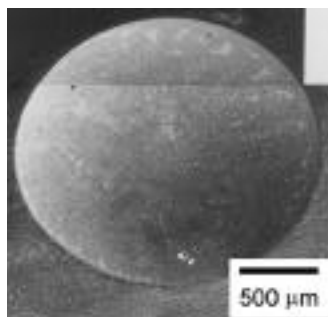
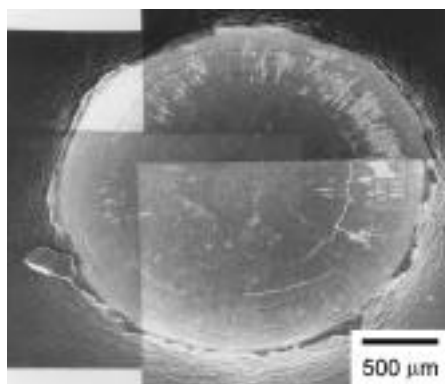


Fig. 2: Specimen geometry

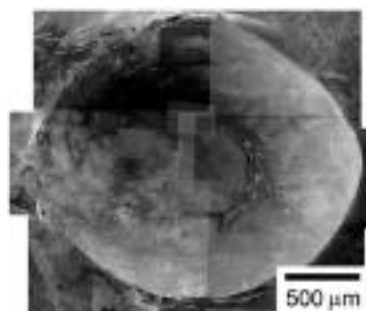


a) 200 m/s

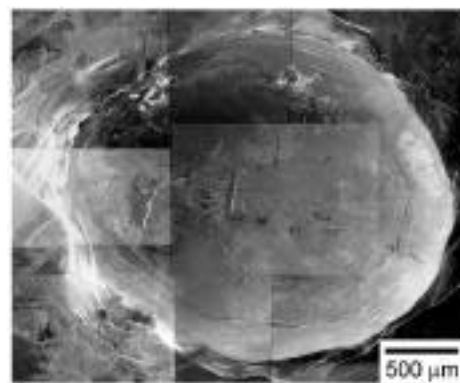


b) 300 m/s

Fig. 3: Bi-modal microstructure. Impact damage sites (SEM),  
Impact conditions: 3.2 mm steel sphere, 90°.

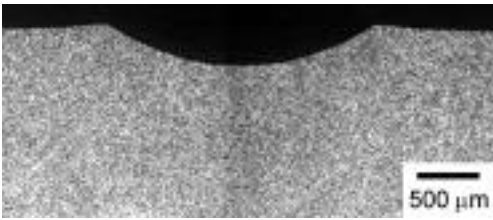


a) 200 m/s

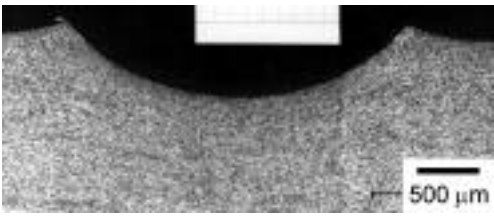


b) 250 m/s

Fig. 4: Lamellar microstructure. Impact damage sites (SEM),  
Impact conditions: 3.2 mm steel sphere, 90°.

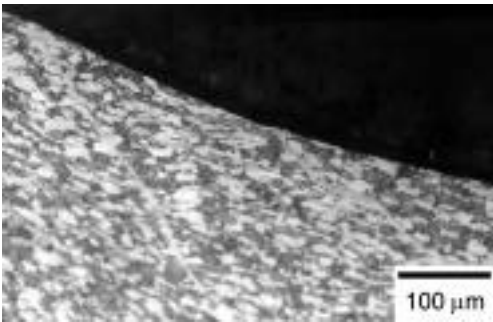


a) 200 m/s

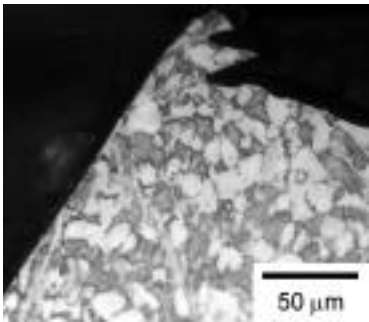


b) 300 m/s

Fig. 5: Bi-modal microstructure. Cross sections of impact craters (LM).  
Impact conditions: 3.2 mm steel sphere, 90°.



a) shear bands at crater bottom



b) crater ridge

Fig. 6: Bi-modal microstructure. Cross sections of impact craters (LM).  
Impact conditions: 3.2 mm steel sphere, 90°, 300 m/s.

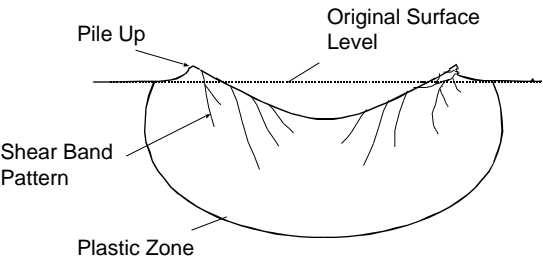


Fig. 7: Schematic cross section of an impact crater.

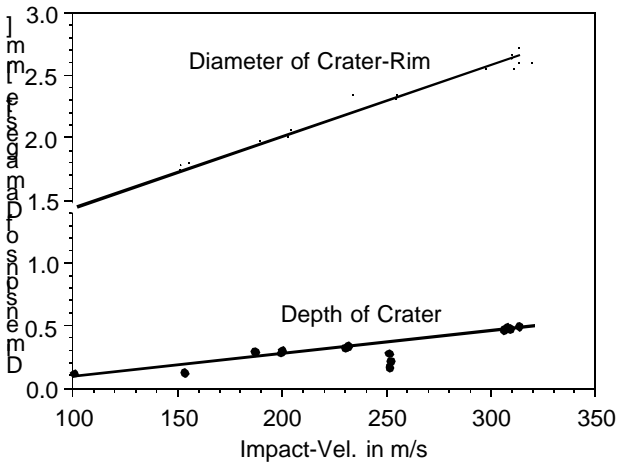


Fig. 8: Bi-modal microstructure. Diameter and depth of impact crater as function of impact velocity.

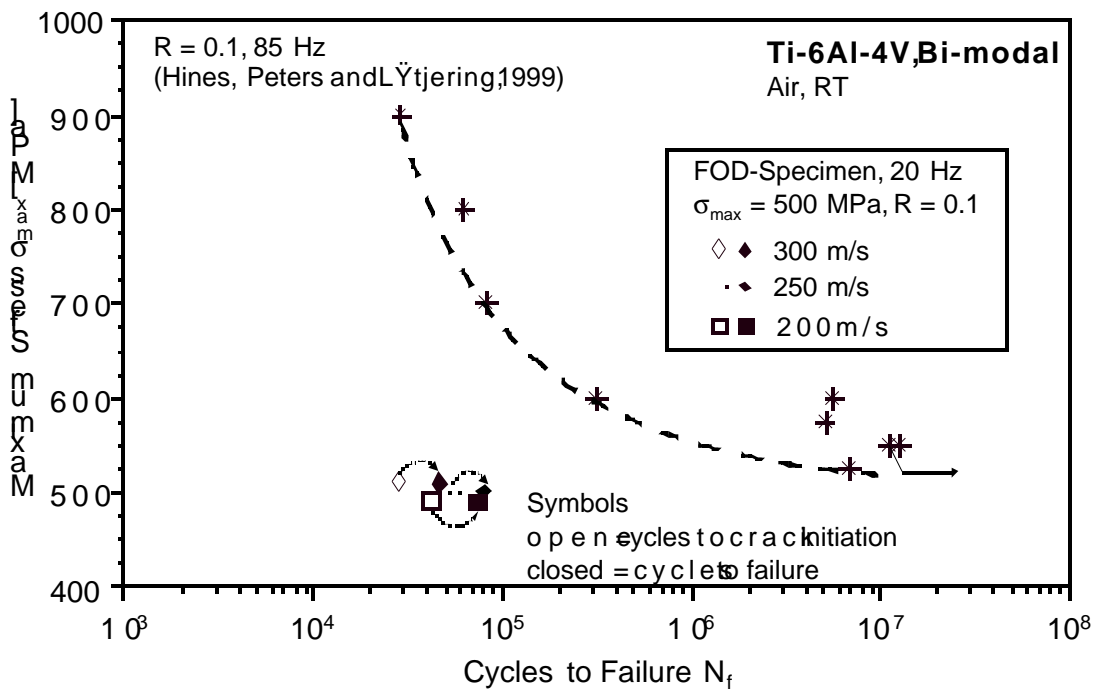
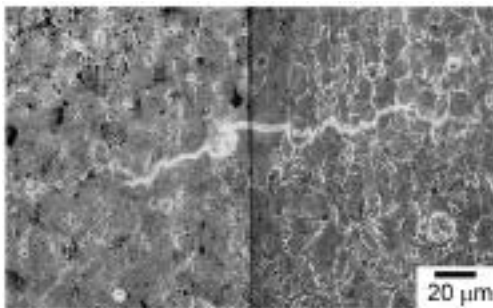


Fig. 9: Bi-modal microstructure. Influence of FOD on fatigue behavior, compared to S-N smooth-bar fatigue data after J.A. Hines, J.O. Peters and G. Lütjering (1999).

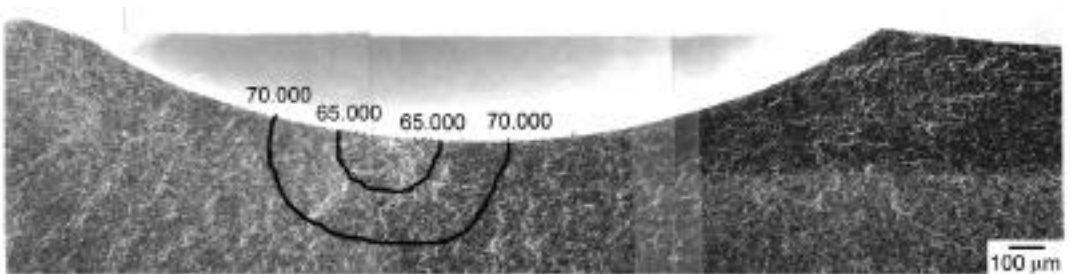


a) 200 m/s impact,  $N = 47.000$  cycles



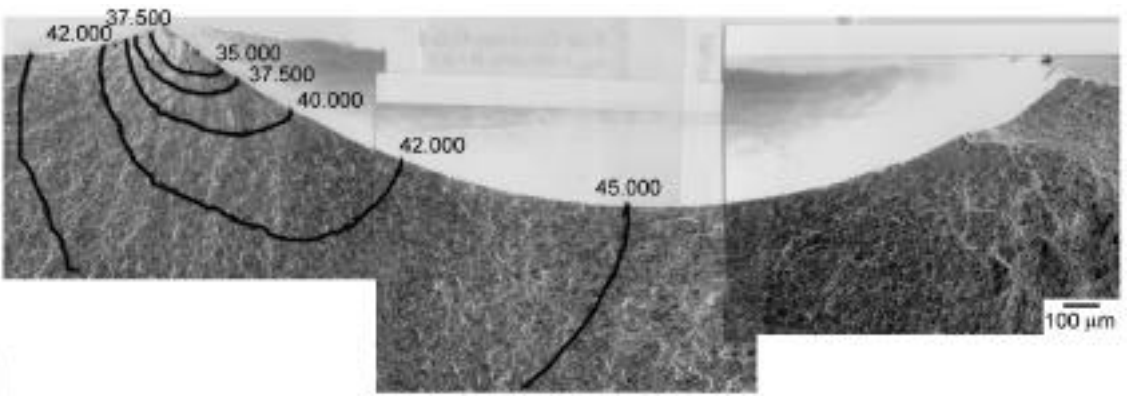
b) 300 m/s impact,  $N = 35.000$  cycles

Fig. 10: Bi-modal microstructure. Crack initiation sites at the specimen surface (SEM):  $\sigma_{max} = 500$  MPa,  $R = 0.1$ , 20 Hz:



a) 250 m/s impact





b) 300 m/s impact

Fig. 11: Bi-modal microstructure. Fracture Surfaces (SEM), Position of crack front as a function of number of cycles during crack extension is shown schematically

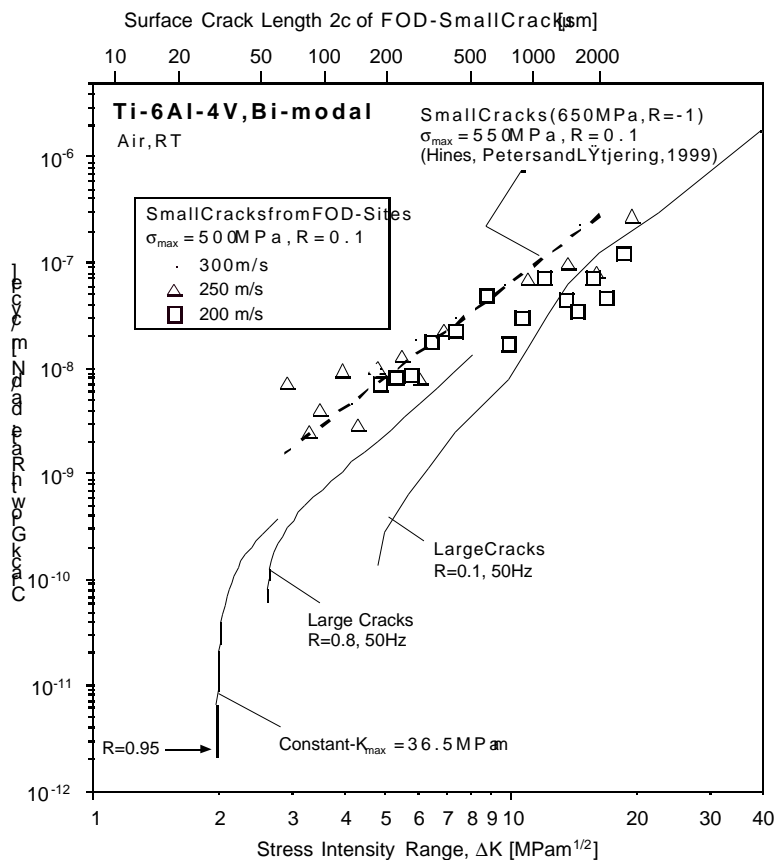


Fig. 12: Bi-modal microstructure. Fatigue crack propagation behavior of small cracks emanating from simulated FOD sites. Comparison with data of naturally initiated small cracks (J.A Hines, J.O. Peters and G. Lütjering, 1999) and large cracks (B.L. Boyce, J.P. Campbell, O. Roder, A.W. Thompson, W.W. Milligan and R.O. Ritchie, 1999).

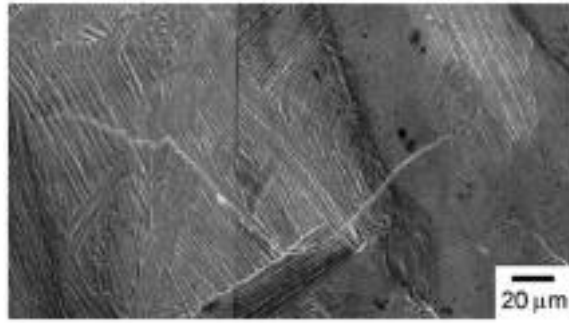


Fig. 13: Lamellar microstructure. Crack initiation site at the specimen surface for a 200 m/s impact (SEM):  $\sigma_{\max} = 500 \text{ MPa}$ ,  $R = 0.1$ , 20 Hz:

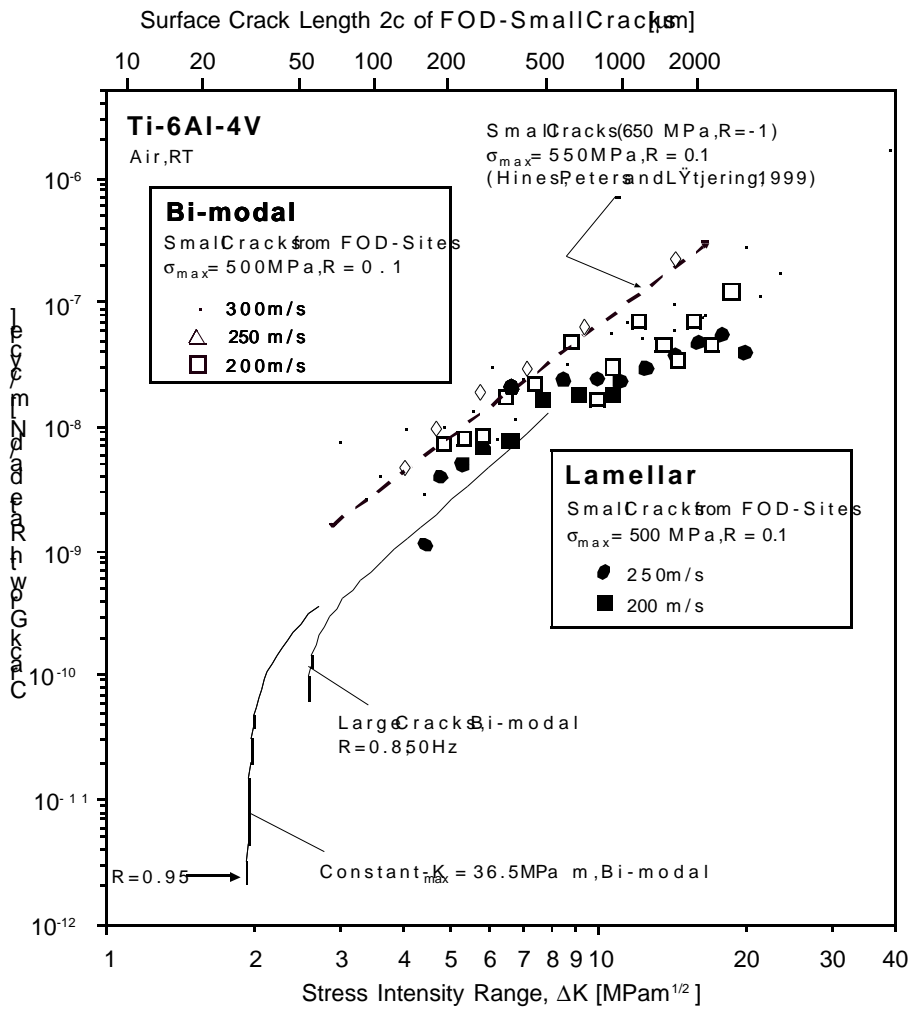


Fig. 14: Fatigue crack propagation behavior of small cracks emanating from simulated FOD sites. Comparison of bi-modal and lamellar microstructures.

## **The Effect and Assessment of Foreign Object Damage to Aero Engine Blades and Vanes**

Mr IF Stewart\*, Rolls-Royce plc, PO Box 31, Derby, DE24 8BJ, UK.

Dr. DP Williams and Dr. D Nowell, Dept. of Engineering Science, University of Oxford, Parkes Rd, Oxford, OX1 3PJ, UK

### **Introduction**

During the course of their lives, aero engines - both military and civil - can ingest foreign objects of various sorts. When birds or ice are ingested, it is generally termed 'soft body' impact, whereas, when stones, rivet mandrels, bits of tyre, clipboards etc, are ingested, it is termed 'hard body' ingestion and the damage it causes is called Foreign Object Damage or FOD.

FOD can cause significant amounts of damage to the blades and vanes in, generally, the compressors of an engine. Indeed, should a nick in a leading (or trailing) edge of a blade develop into a fatigue crack that propagates and fails the blade, then the integrity of the engine and, hence, the aircraft, is put at risk.

Maintenance Manual Limits (MML's) specify the amount of damage that is allowable and how FOD should be treated, as well as the level beyond which the blade (or vane) has to be scrapped. If a blade is redesigned for FOD or any other reason, there is no means, at present, of being able to define the effect this should have on the MML's. This lack of a deterministic method is also important in the inevitable trade-off between the performance and FOD tolerance of a blade in which the aerodynamicist would like a razor blade leading edge and the integrity engineer would like a great thick leading edge that would defeat all FOD but have the aerodynamics of a housebrick.

It should be noted that the whole process of inspection, repair and/or replacement is very costly, with estimates for the UK and US Air Forces, for example, running into many millions of dollars each year - just attributable to FOD. The work described in this paper is the first part of a phased programme to provide a much better understanding of the fundamental mechanisms involved in FOD to blades and to enable generic design rules to be formulated that will enable a design to be assessed and optimised, against any set of conditions in which a blade may suffer from FOD.

In this phase1, the basic methodology for predicting the fatigue life reduction, consequent upon a FOD impact, will be developed and validated on just two, different, types of compressor blade. Phase 2 of the programme will extend the basic methodology developed in phase1 over a much wider range of variables and will, almost certainly, require a test specimen approach. Phase 1 is being carried out at the Department of Engineering Science at Oxford University.

## Experimental Work

### Ballistic Facility

A compressed gas gun was built at Oxford that was capable of firing various missiles at high speeds with a repeatability and accuracy better than the 1 mm required for carrying out the test programme. For the purpose of this programme, the missiles were chosen to be steel balls and the targets were Olympus LP2 blades (Titanium 6-4) and Viper 680 stage 'O' (made in steel). The missile diameters were 4mm and 2mm respectively, though it is planned that other missiles will be used later in the programme.

The speed of the sabot (and therefore the missile) is measured using a timing device at the end of the barrel. After leaving the gun, the sabot hits the sabot-arrestor, which strips away the sabot and leaves the missile to continue its trajectory towards the blade. Figure 1 shows the configuration of the gun.

### Blade Testing

The gun was aimed by inserting, into the end of the barrel, a plug which had two pinholes, 65 mm apart on the centreline. A light was shone down the barrel from the breach end, producing a spot of light on the target blade. The blade was then moved till the spot appeared on the intended impact position.

The trajectory of the missile, in each test, was chosen to be parallel to the direction of rotation of the blade (when in service). It was assumed that the forward velocity of an ingested missile was negligible in comparison with the rotational speed of the compressor blade in a real FOD event. This is a parameter that would be varied in Phase 2 of the whole programme.

### Types of Damage

Previous work (Nicholas et al. 1980) has suggested that there are three broad categories of damage:-

- 1) A dent
- 2) A dent and a tear or crack
- 3) A piece out

Tests were carried out on the Olympus LP2 blades to see if these damage modes could be reproduced. A suitable impact point was identified about 75 mm up from the root (roughly one quarter of the way up the blade), with the blade in first flap, from a dynamic finite element analysis of the blade.

Impacts on the leading edge at this position resulted in a simple dent being produced at just below 280 m/sec, see Fig 2 and a dent with a 'U'-shaped crack on the back of the blade, with an

impact velocity of about 300 m/sec, Fig 3. A complete piece out resulted from velocities above 350 m/sec, Fig 4.

## Fatigue Testing

Once it was demonstrated that the different types of damage could be recreated, five blades of each damage type were fatigue tested by the Experimental Vibration Laboratory at Rolls-Royce plc, Bristol. In every case a fatigue crack was seen to initiate from the damage zone and propagate in a straight line across the blade towards the trailing edge. The tests were stopped when the frequency had dropped by 2% and so the blades were left in one piece. The number of cycles to failure enabled a comparison to be made between the three types of damage. It was observed that the 'dent and tear' category of damage was most detrimental to fatigue life. The other two categories had fatigue lives similar to each other.

## Further Experimental Work

A very different type of blade, the Viper 680 stage '0' compressor blade is now being tested in a similar way to the Olympus LP2 blades. The Viper blade is much smaller, has a thinner leading edge and includes snubbers.

## Numerical Modelling

In order to assess the specific effects of specific types of damage, it is perfectly feasible to carry out a test programme that would provide the answers. However, the approach that Rolls-Royce is taking is to try and get a deeper understanding of the impact mechanisms, as well as the features that exist within the plastically deformed metal, that, in the presence of a vibrating centrifugal stress field, lead to a crack that then propagates to reduce the fatigue life of the blade (or vane) - and it is believed that the best way to achieve this is by sophisticated, numerical modelling.

It was decided to use the explicit finite element code Dyna 3D to model the impact experiments. Dyna 3D has been used to model many impact situations and was already used by Rolls-Royce to model such things as bird ingestion and the behaviour of engine casings under blade-off impact loading.

## Finite Element Mesh

The mesh was set up to give a very fine grid in and around the impact area, becoming progressively more coarse at points further away from the impact. To decrease the number of elements required in the analysis, only part of the blade was meshed. A simple calculation using the Young's Modulus, density and approximate duration of impact, suggested that elastic waves would travel a maximum of 55 mm during the impact of the blade so, a region of at least 55 mm was meshed around the impact. Six elements were used through the thickness of the blade to

allow the curvature of the leading edge of the blade to be incorporated with reasonable accuracy. The elements in the impact region are specified as a cube with side length of 0.25 mm.

The geometry of the ball was created by building the spherical shape from a central cube. A six sided lozenge, matching the cube on the inside and the sphere on the outside, was added to each of the six faces of the cube, in order to complete the sphere. The mesh was constructed by meshing the cube and surrounding lozenges separately and matching adjacent nodes to form one complete mesh.

### Boundary Conditions

An initial velocity was given to the ball that matched a given experimental value. In the case of a dent to the leading edge, a velocity of 279 m/s was used. The ball was targeted to hit the leading edge of the blade in exactly the same place as in the experiment. Contact surfaces were created on the ball and the blade to allow Dyna 3D to calculate the behaviour of both solids during the impact event. The “surface-to-surface” type of contact was used in this case.

### Material Properties

For the ball, an elastic material model (Material 1 in Dyna 3D) was used. Values of Young's Modulus, density, and Poisson's Ratio appropriate for steel were taken from engineering tables.

The blade material model was initially chosen as elastic-perfectly plastic (material model 3 in Dyna 3D) and the relevant material properties obtained from the Rolls-Royce material database.

### Results

The results of the numerically simulated impact events were displayed using the postprocessor 'D3Plot'. Figure 5 shows the development of a dent caused by a 279m/s projectile at four different times during the impact that was run for about 60 microseconds. Figure 6 shows the final dent produced by the same impact, and can be compared with that seen in the actual experiment (figure 2).

D3plot also enables a detailed study to be made of the stress and strain distributions around the damage area, helping to give insight into the mechanisms of material failure.

A number of simulations have been carried out at different impact velocities and have been compared with experiment. Good agreement has been established between experimental and numerical impact damage at relatively low velocities, as the denting process involves no material failure other than yield. The Dyna3D material model 3 is less successful at modelling the "dent and tear" and "perforation" damage categories. This elastic-perfectly-plastic model does include a maximum strain failure criterion, where an element is deleted once the strain in the element exceeds a certain critical level. However, this has proved inadequate in the description of failure in our impact events, as elements are seen to fail in both tension and compression. This leads to the unrealistic removal of material directly at the point of impact on the blade.

At present, work is being undertaken to incorporate the Bamman Damage model (Bamman et. al. 1990) into the numerical simulations. This is included in Dyna3D as material 52. This model employs a damage parameter which is a function of a number of quantities, including pressure and effective stress. Elements are deleted when this parameter reaches a value of 1.0. A more detailed description of the model can be found in papers by Bamman (Bamman 1989, Bamman et. al. 1990). The material data was again supplied by RollsRoyce. As with the simple material model, this model is capable of recreating the dents corresponding to low velocity impacts. In a few cases, the model has also exhibited the general 'U,-shaped tear seen on the back of experimental impacts at intermediate velocities (such as that shown in figure 3). Figure 7 shows the final strain profile in one such case.

For higher velocity impacts that, experimentally, cause perforations of the leading edge, material 52 has so far been unsuccessful at recreating the damage. Figure 8 shows the Dyna3D model of a higher velocity impact. A large, straight tear is seen to develop from the leading edge, rather than a semi-circular perforation. There is some evidence that the crack direction is dependent on the mesh, indicating that a much smaller element size is required in the impact region.

## **Conclusions**

The gas gun, developed at Oxford, is able to reproduce the three types of damage observed by Nicholas et. al. (1980) and found in practice, when blades are removed from engines after FOD events.

Fatigue tests have shown the 'dent with tear' damage type to be the most detrimental to the fatigue life of the blade when vibrated in 'first flap' mode.

The Dyna3D finite element models can successfully recreate the impact and subsequent plastic deformation of the material in the damaged area. A damage parameter approach to modelling the material failure associated with higher velocity impacts has shown some agreement with experimental results for dents and small tears but, more work is necessary to describe fully the tearing and perforation of the leading edge.

## Acknowledgements

This project is jointly funded by Rolls-Royce plc and DERA.

## References

A.M.Howatson, P.G.Lund and J.D.Todd (1991): *Engineering Tables and Data (Second Edition)*. Chapman & Hall.

T.Nicholas, J.P.Barber and R.S.Bertke (1980): *Impact Damage on Titanium Leading Edges from Small Hard Objects*. Experimental Mechanics Vol.20, No.10, pp.357-364

D.J.Bamman and E.C.Aifantis (1987): *A Model for Finite Deformation Plasticity*. Acta Mechanica 70, 1-13

D.J.Bamman et. al. (1990): *Predictions of Ductile Failure in Metal Structures*. In AMD-Vol. 107, Failure Criteria and Analysis in Dynamic Response, Edited by H.E.Lindberg, 7-12.

## Ballistic Facility at Oxford University

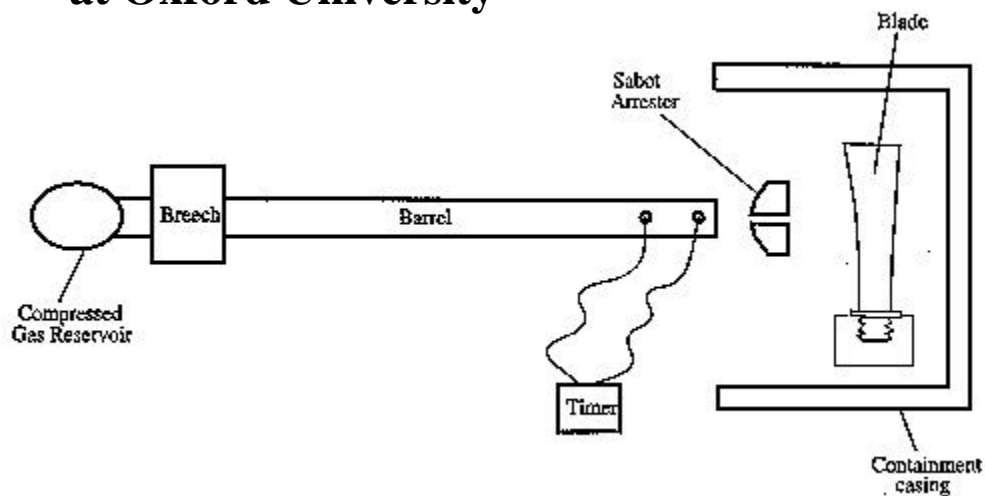
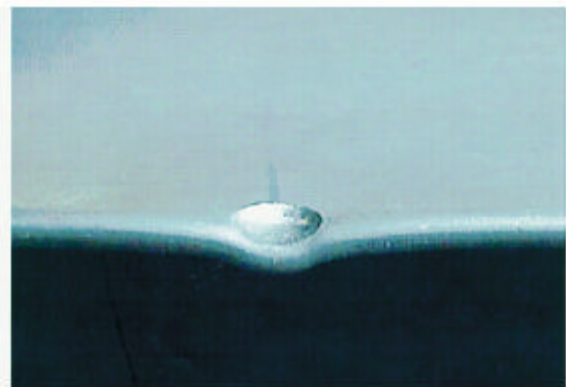


Fig. 1





**Figure 2.** A dent caused by a 279 m/s impact.



**Figure 3.** A 'U' shaped crack on the back of a dent caused by a 300 m/s impact.



**Figure 4.** A complete perforation caused by a 350 m/s impact.

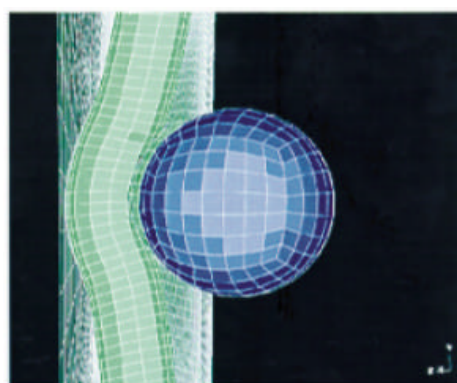
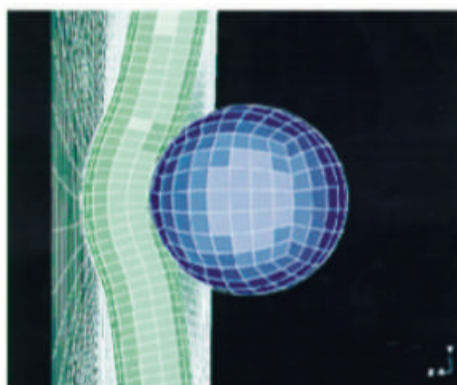
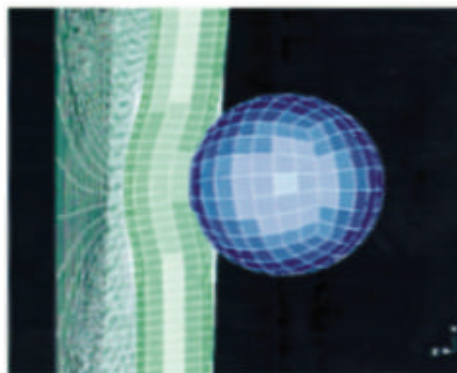
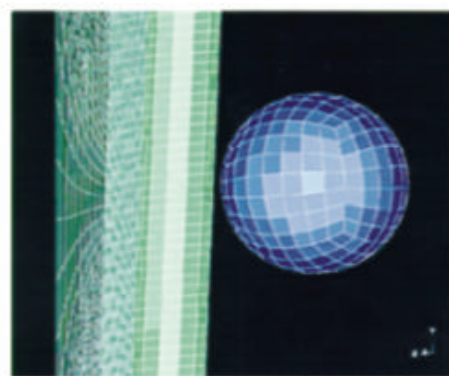


**Figure 5.** The development of a leading edge dent using LS Dyna3D. Steps are  $\sim 20 \mu$  secs.

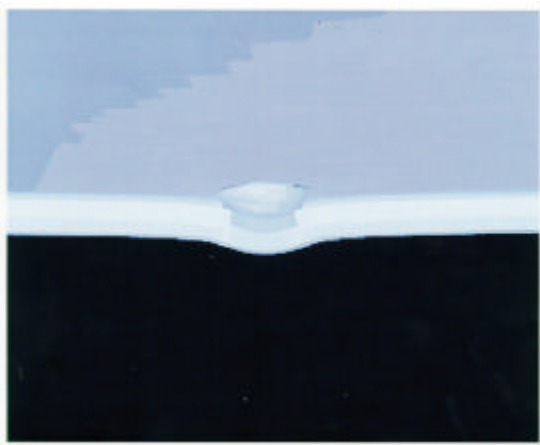


**Figure 6.** The final plastic deformation resulting from a 279 m/s impact.

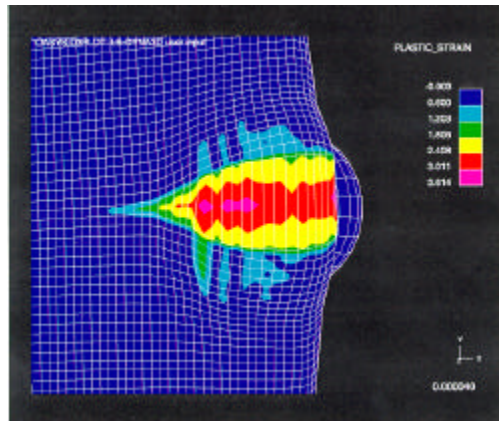


**Figure 8.** A material 52 model of a high velocity (350 m/s) impact. A large tear has formed

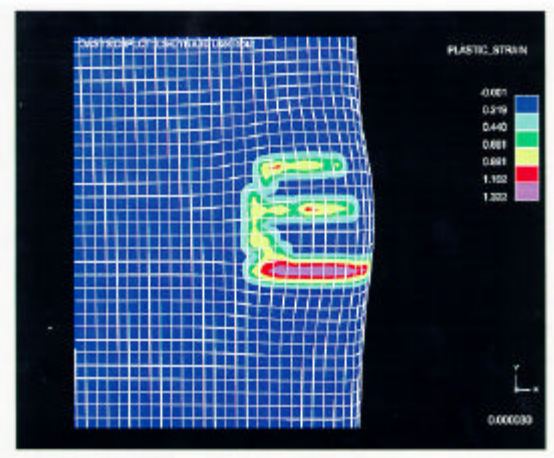


**Figure 7.** A material 52 model of an intermediate (300 m/s) velocity impact. The back of the dent exhibits a 'U' shaped crack.